ELSEVIER

Building resolving large-eddy simulations and comparison with wind tunnel experiments

Piotr K. Smolarkiewicz [a,*], Robert Sharman [a], Jeffrey Weil [b],
Steven G. Perry [c], David Heist [c], George Bowker [d]

[a] *National Center for Atmospheric Research, Boulder, CO 80307, USA*
[b] *University of Colorado, Cooperative Institute for Research in Environmental Science, Boulder, CO 80309, USA*
[c] *Atmospheric Sciences Modeling Division, National Oceanic and Atmospheric Administration, Research Triangle Park, NC 27711, USA*
[d] *Atmospheric Modeling Division, US Environmental Protection Agency, Research Triangle Park, NC 27711, USA*

Abstract

We perform large-eddy simulations (LES) of the flow past a scale model of a complex building. Calculations are accomplished using two different methods to represent the edifice. The first method employs the standard Gal-Chen and Somerville terrain-following coordinate transformation, common in mesoscale atmospheric simulations. The second method uses an immersed boundary approach, in which fictitious body forces in the equations of motion are used to represent the building by attenuating the flow to stagnation within a time comparable to the time step of the model. Both methods are implemented in the same hydrodynamical code (EULAG) using the same nonoscillatory forward-in-time (NFT) incompressible flow solver based on the multidimensional positive definite advection transport algorithms (MPDATA). The two solution methods are compared to wind tunnel data collected for neutral stratification. Profiles of the first- and second-order moments at various locations around the model building show good agreement with the wind tunnel data. Although both methods appear to be viable tools for LES of urban flows, the immersed boundary approach is computationally more efficient. The results of these simulations demonstrate that, contrary to popular opinion, continuous mappings such as the Gal-Chen and Somerville transformation are not inherently limited to gentle slopes. Calculations for a strongly stratified case are also presented to point out the substantial differences from the neutral boundary layer flows.
© 2007 Elsevier Inc. All rights reserved.

Keywords: Urban boundary layers; Terrain-following coordinates; Immersed-boundary approach; Flow past a building

1. Introduction

Recent world events have heightened society's awareness of its vulnerability to the release of chemical and biological agents either through intentional or inadvertent actions. Of particular concern is the release of these

* Corresponding author. Tel.: +1 303 497 8972; fax: +1 303 497 8181.
E-mail address: smolar@ucar.edu (P.K. Smolarkiewicz).

agents in heavily populated urban areas. Thus it becomes a matter of some urgency to be able to detect and forecast the transport and diffusion of hazardous substances in urban areas for effective evacuation and treatment strategies. However, modeling the flows in urban areas around many buildings of different sizes and shapes is an extremely complex problem which taxes the numerical simulation capabilities of both the meteorological and engineering communities. Current approaches to the problem are varied [1], from very simple Gaussian plume semi-empirical estimates through a hierarchy of CFD (computational fluid dynamics) models, with sophisticated large eddy simulations (LES) at the upper end. Recent LES by Liu et al. [2] and Cui et al. [3] are representative of computational studies of neutral planetary boundary layer (PBL) flows past idealized urban street canyons. Both works assume explicit internal boundaries to represent the buildings, while relying on finite-element [2] and finite-volume discretizations [3] of the governing equations.

In general, numerical modeling of natural urban flows is still in its infancy, and because of the tremendous computational burden involved in modeling realistic urban structures, it is important to carefully consider computational efficiency versus accuracy tradeoffs of candidate modeling approaches. In this paper we report on a systematic numerical study of neutrally stratified boundary layer flow over a single complex structure. A unique aspect of our report is a thorough comparison of the model results to independent measurements in a wind tunnel. The structure used is a scale model of the Pentagon building, but the results obtained carry over to other complex constructions which may be embedded in any neutrally stratified urban environment. An example of stratified flow is also included for comparison to the neutral wind tunnel case. The ultimate goal of this research is to develop and identify reliable tools for quantifying the air flow past urban structures under various meteorological conditions.

We conduct building-resolving LES using two distinct methods to represent the edifice. The first method employs the Gal-Chen and Somerville terrain-following coordinate transformation [4] – a standard vertical-coordinate transformation used in many mesoscale atmospheric simulations. In this method, the building is effectively treated as orography, with the resulting slopes truncated according to the adopted grid resolution. The second method uses the immersed boundary approach – originated by Peskin in the area of computational biomechanics [5,6] – in which fictitious body forces in the equations of motion are introduced to represent the internal boundaries; see [7] for a recent review. The particular technique employed here adapts the *feedback forcing* of Goldstein et al. [8], with implicit time discretization admitting rapid attenuation of the flow to stagnation (within the building structure) in $O(\delta t)$ time comparable to the time step δt of the model.

Both methods are implemented in the same hydrodynamical code EULAG[1] widely documented in the literature; cf. [12–15] for recent developments and reviews. The EULAG's underlying numerics are the NFT schemes[2] based on the MPDATA transport algorithms [19,18,20]. The solutions use two different methods for representing the building, but with identical numerics otherwise, and are compared to each other and to wind tunnel data collected for neutral stratification. Profiles of first- and second-order moments at various locations around the building are analyzed, subsequently leading to a synthetic assessment of the efficacy of the two methods. Both approaches show good agreement with the data, and both appear viable tools for LES of urban flows. However, for the case investigated here, the immersed boundary method seems to be slightly more accurate overall and is computationally three times more efficient due to less stringent stability requirements.

A particularly encouraging byproduct of our study is a demonstration that continuous mappings, such as the Gal-Chen and Somerville transformation, are not inherently limited to gentle slopes – an established belief in the geophysical CFD community – and can be quite effective in representing steep urban structures. We point out the technical details of our approach that appear different from those used in traditional atmospheric/oceanic codes, which may be responsible for our successful implementation of the terrain-following coordinates as the orographic slopes approach the vertical. These (details) include particulars of the formula-

---

[1] The name EULAG [9] alludes to the capability to solve the fluid equations in either an Eulerian (flux form [10]) or a Lagrangian (advective form [11]) framework.

[2] The term "nonoscillatory forward-in-time" was introduced in the late nineties [16,17] to label a class of second-order accurate two-time-level algorithms for fluids built on modern nonlinear advection techniques that suppress/reduce/control numerical oscillations characteristic of higher order linear schemes; NFT was meant to distinguish from classical centered-in-time and space linear methods; cf. [18,12] for reviews and discussions.

tion of the elliptic pressure equation, deriving pressure boundary conditions along curvilinear boundaries, and selection of a suitable solver as well as calculation of transformation coefficients by finite-differencing fundamental tensor identities (e.g. "geometric conservation law") rather than evaluating them numerically from the analytic formulae. Although the immersed boundary approach may simplify some of these aspects, it still requires powerful elliptic solvers, as the implicit integrals of the fictitious body forcing translate to abruptly changing coefficients in the elliptic pressure equation. These results have important implications for the use of terrain-following coordinate systems with steep orography common in many geophysical applications.

The remainder of the paper is organized as follows. In the next section, the theoretical formulation of the fluid dynamics model is outlined. The numerical approximations to the governing equations are discussed in Section 3, with some potentially important technical nuances explained in appendices. Design of the numerical experiments and the corresponding results are discussed in Section 4. Remarks in Section 5 conclude the paper.

2. Fluid model: theoretical formulation

The nonhydrostatic model EULAG used in this study has been thoroughly documented in the literature; for recent discussions see [13–15]. In general, EULAG admits several optional formulations of the equations of motion [21,14]. Here, we are concerned with small-scale boundary-layer flows, and thus adopt the classical incompressible Boussinesq approximation. Consequently, we invoke only a small portion of the model's capabilities, thereby simplifying the presentation as well as the computational procedures. The scope of this paper justifies a concise, operator-like symbolic description of the governing equations. Wherever the operator symbols refer to coefficient matrices, they merely indicate matrix operations but do not follow the formalism of matrix algebra to the letter – for a thorough mathematical exposition refer to [13–15].

EULAG's governing equations are formulated (and solved) in transformed time-dependent curvilinear coordinates

$$(\bar{t}, \bar{\mathbf{x}}) \equiv (t, \mathcal{F}(t, \mathbf{x})), \tag{1}$$

with the assumptions that the coordinates $(t, \mathbf{x})$ of the physical domain are orthogonal and stationary – in particular, Cartesian in this paper – and the transformed horizontal coordinates $(\bar{x}, \bar{y})$ are independent of the vertical coordinate z. Given the transformation in (1), the governing equations considered here, can be compactly written as follows

$$\overline{\nabla} \cdot (\rho^* \bar{\mathbf{v}}^s) = 0, \tag{2}$$

$$\frac{d\mathbf{v}}{d\bar{t}} = -\widetilde{\mathbf{G}}\overline{\nabla}\pi' - \mathbf{g}\frac{\theta'}{\theta_b} - \beta\bar{\mathbf{v}} + \mathcal{D}_m(e, \overline{\nabla}\mathbf{v}) - \alpha_m \mathbf{v}' \tag{3}$$

$$\frac{d\theta'}{d\bar{t}} = -\bar{\mathbf{v}}^s \cdot \overline{\nabla}\theta_e - \beta(\theta - \theta_B) + \mathcal{D}_h(e, \overline{\nabla}\theta) - \alpha_h \theta' \tag{4}$$

$$\frac{de}{d\bar{t}} = \mathcal{S}(e) - \beta e \tag{5}$$

where, because of the coordinate transformation, the physical and geometrical aspects are interdependent. Insofar as the physics are concerned: $\mathbf{v}$ denotes the *physical* (i.e., measurable) velocity vector; θ, ρ, and π refer to potential temperature, density, and a density-normalized pressure, respectively; and $\mathbf{g}$ is the acceleration of gravity (vector). The $\mathcal{D}$ terms appearing in the momentum and entropy equations (3) and (4) symbolize viscous dissipation of momentum and diffusion of heat via, respectively, divergence of turbulent stresses and heat fluxes, with corresponding eddy coefficients proportional to the square root of the "turbulent kinetic energy" e whose evolution in (5) symbolizes the standard prognostic "TKE" subgrid-scale model where all usual sinks and sources were combined in the $\mathcal{S}(e)$ term; cf. [17,22] for details. Primes denote deviations from the hydrostatically balanced ambient (i.e., environmental) state $\mathbf{v}_e$, θ_e, and the subscript b refers to the Boussinesq reference state. The relaxation terms with coefficients α and β (functions of the coordinates), appearing on the r.h.s. of (3)–(5), represent fictitious forces whose eventual role is to attenuate the solution to prescribed states within the body of the building (denoted by the subscript B: $\mathbf{v}_B \equiv 0$) and in the vicinity of the open boundaries

of the model, respectively. Notably, all relaxation and viscous terms in the momentum and entropy equations represent parameterizations justified by expediency and, ultimately, by comparison with data.

The geometry of the coordinates in (1) enters the governing equations as follows: in the mass continuity equation (2), $\rho^* \equiv \rho_b \overline{G}$ with $\overline{G}$ denoting the Jacobian of the coordinate transformation; whereas in the momentum equation (3), $\widetilde{G} \sim (\partial \overline{x}/\partial x)$ symbolizes the renormalized Jacobi matrix of the transformation coefficients; $\overline{\nabla} \cdot \equiv \partial/\partial \overline{x} \cdot$, and the total derivative is given by $d/d\overline{t} \equiv \partial/\partial \overline{t} + \overline{v}^* \cdot \overline{\nabla}$, where $\overline{v}^* \equiv d\overline{x}/d\overline{t} \equiv \dot{\overline{x}}$ is the *contravariant velocity*. Appearing in the continuity (2) and entropy (4) equations is the *solenoidal velocity*

$$\overline{v}^s \equiv \overline{v}^* - \frac{\partial \overline{x}}{\partial t}, \tag{6}$$

that follows [23] from the generic (tensor invariant) form of incompressible continuity equation

$$\overline{G}^{-1} \left(\frac{\partial \rho^*}{\partial \overline{t}} + \overline{\nabla} \cdot (\rho^* \overline{v}^*) \right) \equiv 0. \tag{7}$$

The transformation

$$\overline{v}^s = \widetilde{G}^T v. \tag{8}$$

relates the solenoidal and physical velocities directly. For further details of the metric and transformation tensors as well as the formulation of the viscous and dissipative terms in the governing equations, the interested reader is referred to [15] and references therein.

Following [14], the general dependence of $\overline{z}$ on (x, y, z, t) in (1) collapses to a similarity transformation

$$\overline{z} = \mathcal{C}(\xi)$$
$$\xi = \xi(x, y, z, t) := H_0 \frac{z - z_s(x, y, t)}{H(x, y, t) - z_s(x, y, t)}, \tag{9}$$

where H and z_s are the upper and lower surface elevations, respectively, H_0 denotes the vertical extent of the transformed model domain, and the function $\mathcal{C}$ conveniently admits a class of vertically stretched coordinates. The transformation in (9) is a generalization of the classical terrain-following Gal-Chen and Somerville [4] transformation. It has the computational advantage of separability into one- and two-dimensional fields. In particular, the Jacobian of the transformation is given as

$$\overline{G} = \left(\frac{d\mathcal{C}}{d\xi} \frac{\partial \xi}{\partial z} \right)^{-1} \left(\frac{\partial \overline{x}}{\partial x} \frac{\partial \overline{y}}{\partial y} - \frac{\partial \overline{x}}{\partial y} \frac{\partial \overline{y}}{\partial x} \right)^{-1} \equiv \left(\frac{d\mathcal{C}}{d\xi} \right)^{-1} \overline{G}_0 \overline{G}_{xy}, \tag{10}$$

with

$$\overline{G}_0 \equiv \left(\frac{\partial \xi}{\partial z} \right)^{-1} = \frac{H(x, y, t) - z_s(x, y, t)}{H_0}. \tag{11}$$

Throughout this paper, $\overline{x} = x$, $\overline{y} = y$ and $\xi = \overline{z}$; thereby employing the identity transformation in the horizontal (viz. $\overline{G}_{xy} \equiv 1$). Furthermore, the upper boundary is stationary and flat (viz. $H \equiv H_0$), and there is no vertical stretching of the lower-boundary-fitted coordinate $\overline{z}$ (viz. $d\mathcal{C}/d\xi \equiv 1$). The lower boundary is also stationary but inhomogeneous, $z_s = z_s(x, y)$, thereby reducing (9) to the classical case, standard in many atmospheric/oceanic models. In spite of the resulting mathematical simplifications, the actual EULAG program accommodates (1) and (9) in their full generality. We retain the consistent notation for conciseness of forthcoming discussions and ease of connection to earlier works.

3. Numerical approximations

Given (7), each prognostic equation that forms the Boussinesq system (3)–(5) can be written in two equivalent forms, either as a Lagrangian evolution equation

$$\frac{d\psi}{d\overline{t}} = R, \tag{12}$$

or an Eulerian conservation law

$$\frac{\partial \rho^* \psi}{\partial \bar{t}} + \overline{\nabla} \cdot (\rho^* \bar{\mathbf{v}}^* \psi) = \rho^* R. \tag{13}$$

Here ψ symbolizes components of $\mathbf{v}$ as well as θ' or e, and R denotes the associated r.h.s.

We approximate either (13) or (12) to second-order accuracy in space and time using the nonoscillatory forward-in-time (NFT) approach – see [18,12] for reviews and discussions. The particular NFT algorithm employed here can be formally written as

$$\psi_{\mathbf{i}}^{n+1} = LE_{\mathbf{i}}(\tilde{\psi}) + 0.5\delta t R_{\mathbf{i}}^{n+1} \equiv \hat{\psi}_{\mathbf{i}} + 0.5\delta t R_{\mathbf{i}}^{n+1}; \tag{14}$$

where $\psi_{\mathbf{i}}^{n+1}$ is the solution sought at the grid point $(\bar{t}^{n+1}, \bar{\mathbf{x}}_{\mathbf{i}})$, $\tilde{\psi} \equiv \psi^n + 0.5\delta t R^n$, and LE denotes a two-time-level either advective semi-Lagrangian [11] or flux-form Eulerian [10] NFT transport operator, viz. advection scheme.[3] The calculations reported in this paper used exclusively the second-order-accurate, monotone (FCT) [24], flux-form scheme MPDATA, the technical details of which are widely described in the literature; see [19,18,20] and references therein. For the reader's convenience and clarity of the following discussion, we outline the functional form of MPDATA in Appendix A.

Subgrid-scale (SGS) forcings $\mathcal{D}_m$, $\mathcal{D}_h$ and S – in (3)–(5), respectively – included in R are evaluated explicitly and to first-order. This is justified because they enter the equations of motion only as a consequence of a subgrid-scale turbulence model, already as $\sim \mathcal{O}(\delta x^2)$ corrections. Technically, this eliminates the need for predicting SGS^{n+1} in R^{n+1} on the r.h.s. of (14), as $SGS(\psi^{n+1}) = SGS(\psi^n) + \mathcal{O}(\delta t)$. Programming wise, the definition of the auxiliary field $\tilde{\psi}$ is expanded as $\tilde{\psi} \equiv \psi^n + 0.5\delta t(R_{\text{rsv}}^n + 2R_{\text{sgs}}^n)$, while accounting only for the resolved forcing R_{rsv} in R^{n+1} on the r.h.s. of (14); cf. Sections 3.5.4 and 4.2 in [18] for discussion. The explicit first-order evaluation of SGS forcings improves the efficacy of the calculations. When required however, it can be extended to a trapezoidal integration, employed for the resolved forcing R_{rsv}, by means of an outer iteration scheme [25].

The template algorithm (14) already incorporates the assumption that all prognostic variables are defined at the same grid points $\bar{\mathbf{x}}_{\mathbf{i}}$. This is important for the efficacy of the model; see [9] for a discussion. In EULAG we allow two grid configurations: the unstaggered A-grid, where all variables are defined at the same positions, and the staggered B-grid, where a pressure variable is staggered one-half grid interval in all directions with respect to the other variables [26]. In either case, advection and diffusion modules mimic a staggered C-grid with fluxes evaluated at fictitious cell-wall locations surrounding data points $\bar{\mathbf{x}}_{\mathbf{i}}$, cf. Appendix A; whereas partial derivatives $\partial/\partial\bar{\mathbf{x}}$ composing the Nabla operator $\overline{\nabla}$ on the l.h.s. of (2) as well as in the pressure gradient and convective-derivative terms, respectively, on the r.h.s. of (3) and (4) are approximated with standard second-order-accurate finite-difference formulae. All calculations reported in this paper were performed on the A-grid.

Note that Eq. (14) represents a system implicit with respect to all resolved variables in (3) and (4), because the velocity components, pressure, and potential temperature are assumed to be unknown at $n + 1$. For the physical velocity vector $\mathbf{v}$, it can be written compactly as

$$\mathbf{v}_{\mathbf{i}} = \hat{\mathbf{v}}_{\mathbf{i}} - 0.5\delta t (\tilde{\mathbf{G}}(\overline{\nabla}\pi'))_{\mathbf{i}} + 0.5\delta t \mathbf{R}_{\mathbf{i}}(\mathbf{v}, \hat{\theta}'), \tag{15}$$

where

$$\mathbf{R}_{\mathbf{i}}(\mathbf{v}, \hat{\theta}') \equiv -(\beta \mathbf{v} + \alpha_m(\mathbf{v} - \mathbf{v}_e))_{\mathbf{i}} - \mathbf{g}\frac{1}{\theta_0}\frac{\hat{\hat{\theta}}_{\mathbf{i}}' - 0.5\delta t((\tilde{\mathbf{G}}^{\mathrm{T}}\mathbf{v}) \cdot \overline{\nabla}\theta_e)_{\mathbf{i}}}{1 + 0.5\delta t(\beta + \alpha_h)_{\mathbf{i}}}, \tag{16}$$

with

$$\hat{\hat{\theta}}' \equiv \hat{\theta}' + 0.5\delta t \beta(\theta_{\mathrm{B}} - \theta_e), \tag{17}$$

accounts for the implicit representation of the buoyancy and relaxation forcings via (4), and the superscript $n + 1$ has been dropped as there is no ambiguity. On grids unstaggered with respect to all prognostic variables,

---

[3] The flux-form Eulerian transport operator LE invokes the multiplicative factor ρ^{*n}/ρ^{*n+1} to account for time variability of the generalized density ρ^* due to coordinate dependence on time, see [12] for discussion.

(15) can be inverted algebraically (viz. locally) to construct expressions for the solenoidal velocity components that are subsequently substituted into (2) to produce an elliptic equation for pressure

$$\left\{ \frac{\delta t}{\rho^*} \overline{\nabla} \cdot \rho^* \widetilde{\mathbf{G}}^{\mathrm{T}} [\hat{\mathbf{v}} - (\mathbf{I} - 0.5 \delta t \hat{\mathbf{R}})^{-1} \widetilde{\mathbf{G}} (\overline{\nabla} \pi'')] \right\}_i = 0, \tag{18}$$

where $\widetilde{\mathbf{G}}^{\mathrm{T}} [\hat{\mathbf{v}} - (\mathbf{I} - 0.5 \delta t \hat{\mathbf{R}})^{-1} \widetilde{\mathbf{G}} (\overline{\nabla} \pi'')] \equiv \bar{\mathbf{v}}^s$ defined in (6). In (18), $\hat{\mathbf{v}}$ combines all explicit parts on the r.h.s. of (15) – so, $\hat{\mathbf{R}}$ denotes the resulting linear (homogeneous) operator acting on $\mathbf{v}$ – and $\pi'' \equiv 0.5 \delta t \pi'$; cf. [13] for the complete development. Boundary conditions imposed on $\bar{\mathbf{v}}^s \cdot \mathbf{n}$, subject to the integrability condition $\int_{\partial\Omega} \rho^* \bar{\mathbf{v}}^s \cdot \mathbf{n} d\sigma = 0$, imply the appropriate boundary conditions on π'' [13,14]; for additional particulars see Appendix B. The resulting boundary value problem is solved – with accuracy to a judiciously specified threshold $\|(\delta t / \rho^*) \overline{\nabla} \cdot \rho^* \bar{\mathbf{v}}^s\| < \varepsilon$, see [16] for a discussion – using a preconditioned generalized conjugate residual GCR algorithm [27–29], a nonsymmetric Krylov subspace solver akin to the popular generalized minimum residual GMRES scheme, [27,30]. Given the updated pressure, and hence the updated solenoidal velocity, the updated physical and contravariant velocity components are constructed from the solenoidal velocities using the transformations (8) and (6), respectively.

The detailed form of the transformation coefficients – i.e., the entries of $\widetilde{\mathbf{G}}$ appearing throughout (3), (8), and (18) – was given in [13–15]. Here we only emphasize that – in contrast to the majority of atmospheric/oceanic models using the Gal-Chen and Somerville transformation – we evaluate the coefficients by differentiating the Jacobians $\overline{G}_0$, defined in (11), rather than using direct differentiation of z_s; see section 2.2 in [14] for an exposition. This aims at satisfying the fundamental tensor identities [15,31] at the finite difference level. In our experience, this approach minimizes the production of spurious vorticity at the curvilinear boundaries and accelerates convergence of the elliptic solver.

4. Experimental setup

The wind tunnel experiment, Fig. 1, was conducted in the US EPA Meteorological Wind Tunnel at the Fluid Modeling Facility; the laboratory setup is highlighted in Fig. 2. It employs a 1:200 scale model of the building, with a large scale neutrally stratified ambient (free-stream) flow $\mathbf{v}_e = (U_0, 0, 0)$ where $U_0 \approx 4 \text{ m s}^{-1}$. With the characteristic length scale of the model $L = 2 \text{ m}$, this gives a Reynolds' number $Re \approx 5 \times 10^5$, only two orders of magnitude lower than for natural atmospheric boundary layer flows. The experimental
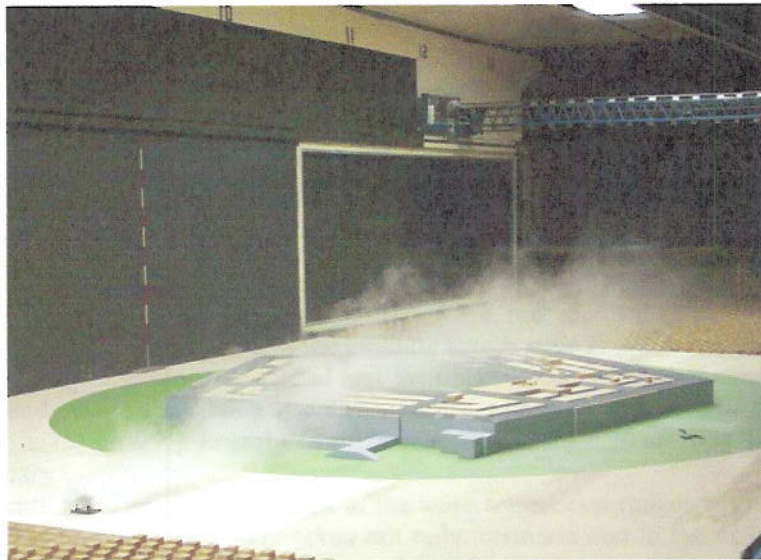

Fig. 1. Smoke visualization of point source plume around 1:200 scale model in the Meteorological Wind Tunnel.

Although both solutions seem qualitatively similar, there are some apparent differences. For instance, the IMB solution evinces more activity within the building courtyard and produces a more intense but narrower wake. Because the simulated flow is turbulent and intermittent – with the magnitude of the fluctuations comparable to that of the ambient flow – contrasting instantaneous results can be misleading. To better expose global differences between the IMB and GCT solutions, Fig. 6 juxtaposes the corresponding time-averaged $\langle w \rangle$ fields. Except for stronger updrafts/downdrafts at the flanks of the building in the IMB result, both results appear to match closely, and without reference to the measurements it seems impossible to judge which solution is more realistic.

The wind tunnel LDV measured vertical profiles include: profiles of the averaged velocity components $\langle u \rangle$, $\langle v \rangle$, $\langle w \rangle$; the component variances, e.g. $\langle u'u' \rangle \equiv \langle u - \langle u \rangle \rangle^2$ as well as their sum (0.5×, viz. the kinetic energy k' of velocity fluctuation); and two Reynolds' fluxes $\langle u'v' \rangle$ and $\langle u'w' \rangle$. With these nine profiles measured at 41 sites, cf. Fig. 3, a detailed comparison of the various runs with the data is not possible to present here. Below we summarize our overall experience with the simulation approaches, illustrated with selected results.

Tables 2–6 present the root mean square (RMS) error statistics for the measured first- and second-order normalized moment variables, derived by comparison to the wind tunnel LDV measurements for both the IMB and GCT methods at sites (cf. Fig. 3) representative of the following locations: 1 for upstream; 23 for lateral flanks; 7 for courtyard; 11 for rooftop; and 15 for wake. The calculated RMS error of the profile is
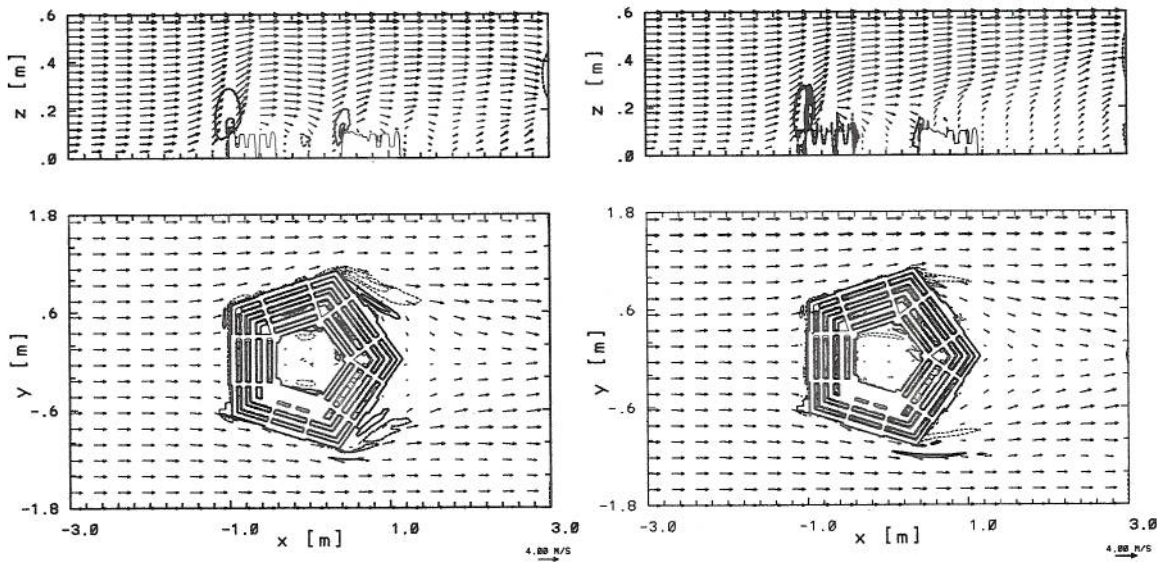

Fig. 6. Time-averaged vertical velocity fields $\langle w \rangle$ for IMB (left plates) and GCT (right plates); contour intervals and arrow lengths are the same as in Figs. 4 and 5.

Table 2
RMS error statistics of first- and second-order normalized moment variables for the IMB and GCT calculation methods compared to the normalized wind tunnel data (WAV and WMX for vertically averaged and maximal values) at site 1 upstream of the building

Src.	u	v	w	$u'u'$	$v'v'$	$w'w'$	$k'k'$	$u'v'$	$u'w'$
IMB	1.289	0.044	0.081	1.134	0.935	0.786	1.161	0.141	0.543
GCT	1.259	0.049	0.091	1.134	0.935	0.786	1.161	0.141	0.543
WAV	6.163	0.039	0.306	1.130	0.934	0.784	1.158	−0.013	−0.541
WMX	7.873	0.100	0.377	1.218	0.980	0.870	1.227	0.207	0.588

Square-roots of the magnitude of second-order moments are shown, for direct comparability with first-order fields; and all numerical entries are multiplied by 10, for compactness. See text for precise definitions.

Table 3
As in Table 2 but for site 23 on a lateral flank

Src.	u	v	w	$u'u'$	$v'v'$	$w'w'$	$k'k'$	$u'v'$	$u'w'$
IMB	1.032	0.301	0.440	1.066	0.922	0.748	1.123	0.331	0.515
GCT	0.978	0.131	0.355	1.042	0.922	0.747	1.115	0.331	0.515
WAV	6.795	0.388	0.481	1.093	0.923	0.748	1.138	0.323	−0.517
WMX	8.329	1.008	0.670	1.166	1.015	0.872	1.169	0.400	0.560

Table 4
As in Table 2 but for site 7 in the courtyard

Src.	u	v	w	$u'u'$	$v'v'$	$w'w'$	$k'k'$	$u'v'$	$u'w'$
IMB	0.855	0.124	0.262	0.844	0.829	0.729	0.872	0.349	0.671
GCT	1.631	0.257	0.153	1.385	0.931	0.786	1.467	0.419	0.660
WAV	4.723	0.052	−0.225	1.610	0.959	0.808	1.630	0.201	−0.595
WMX	8.266	0.160	0.414	1.962	1.046	0.931	1.946	0.258	0.773

Table 5
As in Table 2 but for site 10 at a rooftop

Src.	u	v	w	$u'u'$	$v'v'$	$w'w'$	$k'k'$	$u'v'$	$u'w'$
IMB	0.717	0.108	0.254	1.023	0.776	0.738	0.972	0.414	0.674
GCT	2.165	0.143	0.235	1.446	0.996	0.887	1.537	0.239	0.520
WAV	6.086	0.078	0.378	1.660	1.098	1.002	1.696	0.186	−0.702
WMX	8.193	0.244	0.881	2.034	1.358	1.285	2.119	0.330	0.928

Table 6
As in Table 2 but for site 15 in the wake of the building

Src.	u	v	w	$u'u'$	$v'v'$	$w'w'$	$k'k'$	$u'v'$	$u'w'$
IMB	0.471	0.122	0.291	0.739	0.580	0.275	0.597	0.305	0.249
GCT	1.515	0.102	0.323	1.017	0.723	0.762	1.033	0.354	0.728
WAV	4.680	0.058	0.238	1.367	1.152	1.054	1.466	0.139	−0.816
WMX	7.783	0.233	0.731	1.655	1.267	1.169	1.660	0.343	0.951

the average over the four grid points surrounding each site location at all vertical positions measured by the LDV. To avoid ambiguity, we write the adopted formulae explicitly. First we evaluate

$$\delta\xi = \sqrt{\frac{1}{N_v}\sum_{k=1}^{N_v}(\tilde{\xi} - \overline{\xi})^2} \tag{19}$$

where ξ refers to normalized measured profiles – e.g., $\langle u \rangle / U_0$ or $\langle u'w' \rangle / U_0^2$ – N_v is the number of vertical positions measured by the LDV (in general, different for each site), the tilde refers to the average over the 4 grid points surrounding each measurement, and the overbar denotes the measured profile. Next, for the second-order moments all numerical entries in the tables are transformed according to

$$\delta\xi^* = \mathrm{sgn}(\delta\xi)\sqrt{|\delta\xi|}, \tag{20}$$

to facilitate relating the magnitude of the fluctuations to the means. Finally, all numerical entries in the tables are premultiplied by the factor of ten, for the sake of compactness. The first column denotes the data source, either from calculations or measurements. Both WAV and WMX refer to wind tunnel measurements; denoting, respectively, the vertically averaged and maximal values of the profile. Together, the two characteristics aid in assessing "wiggliness" of fields with averages close to zero.
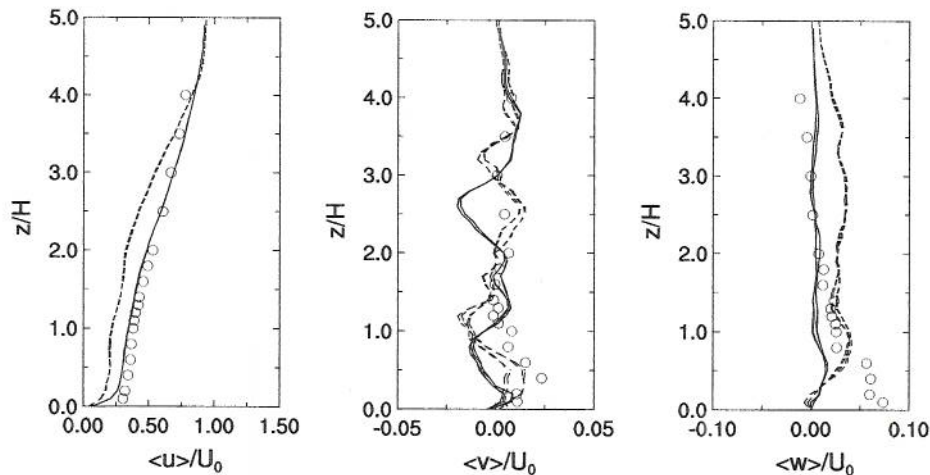
Fig. 7. Vertical profiles of mean velocity components in the building wake at site 15 (leeward most site at $x/H = 21$ and $y/H = 0$ in Fig. 3). Solid and dashed lines are for the IMB and GCT calculations, respectively, for the four grid points surrounding the LDV wind tunnel measurements (open circles).

As illustrated in the Tables, overall, the IMB technique provides slightly smaller RMS errors for most stations, but this trend is not universal and depends on the actual location and quantity being compared. In general, the mean profiles of the velocity components compare with measurements reasonably well for both IMB and GCT calculations. This is illustrated in Fig. 7 that displays the normalized mean profiles of $\langle u \rangle$, $\langle v \rangle$, and $\langle w \rangle$ at Site 15 (the leeward most site at $y = 0$ in Fig. 3). For the streamwise velocity component the IMB is more accurate up to $z = 3\,h$; whereas for the vertical velocity component, the IMB appears more accurate above $z = 2\,h$, while both simulations underpredict the measured weak updraft below about $z = 0.5\,h$. This is, however, not a global trend but only a local deviation, as at Site 12 (not shown) both calculations capture the low-level updrafts equally well, while overpredicting the vertical velocity at $z > 2\,h$.

Insofar as the fluctuation fields are concerned, both simulation techniques capture the magnitude and overall vertical structure of the measured profiles. For illustration, Fig. 8 shows, again for Site 15, profiles of velocity component variances, their sum (0.5×), and the Reynolds fluxes. Although the IMB appears more accurate in some respects, there is no clear indication that it is uniformly superior to the GCT. Noteworthy, upwind of the building both simulations depart from the data to the same degree, predicting, in essence, no turbulent fluctuations. Since the amplitude of the measured fluctuations upwind of the building is roughly only twice smaller than in the lee, this cannot be attributed to wind tunnel noise. Our attempts to mimic the background wind-tunnel turbulence by introducing roughness blocks (cf. Figs. 1 and 2), allowing for adequate noise at the inflow boundary, or initializing subgrid-scale e with the $\langle k'k' \rangle$ profile measured at Site 1 (at the downwind edge of the upwind strip of roughness blocks) all failed to reproduce the measured fluctuation fields upwind of the building. We tend to believe that this is not due to an inadequacy of numerical model per se, but due to the unavailability of the actual initial and/or boundary conditions. Also, it should be remembered that the length of time averaging of the simulated fields is much less than in the wind tunnel. Based on our analysis of the experiments with shorter time averaging (not shown), longer time averages would provide closer agreement.

6. Strongly stratified flow regime

Although wind tunnel experiments of flow over blocks and other obstacles to represent buildings and street canyons are ongoing, e.g. [37,38], their utility is limited mainly to neutral stratification and unidirectional flow. Some stratified wind tunnel and towing tank measurements have been made, e.g. [39–41,43,42], but used simplified thermal structures and elementary obstacle shapes. These configurations may not always be representative of actual atmospheric flows in urban areas. For example, Frehlich et al. [44] using lidar profiling of the urban/suburban boundary layer in the Washington, DC area, show a wide variety of atmospheric conditions,

Building resolving large-eddy simulations and comparison with wind tunnel experiments

Piotr K. Smolarkiewicz [a,*], Robert Sharman [a], Jeffrey Weil [b],
Steven G. Perry [c], David Heist [c], George Bowker [d]

[a] *National Center for Atmospheric Research, Boulder, CO 80307, USA*
[b] *University of Colorado, Cooperative Institute for Research in Environmental Science, Boulder, CO 80309, USA*
[c] *Atmospheric Sciences Modeling Division, National Oceanic and Atmospheric Administration, Research Triangle Park, NC 27711, USA*
[d] *Atmospheric Modeling Division, US Environmental Protection Agency, Research Triangle Park, NC 27711, USA*

Abstract

We perform large-eddy simulations (LES) of the flow past a scale model of a complex building. Calculations are accomplished using two different methods to represent the edifice. The first method employs the standard Gal-Chen and Somerville terrain-following coordinate transformation, common in mesoscale atmospheric simulations. The second method uses an immersed boundary approach, in which fictitious body forces in the equations of motion are used to represent the building by attenuating the flow to stagnation within a time comparable to the time step of the model. Both methods are implemented in the same hydrodynamical code (EULAG) using the same nonoscillatory forward-in-time (NFT) incompressible flow solver based on the multidimensional positive definite advection transport algorithms (MPDATA). The two solution methods are compared to wind tunnel data collected for neutral stratification. Profiles of the first- and second-order moments at various locations around the model building show good agreement with the wind tunnel data. Although both methods appear to be viable tools for LES of urban flows, the immersed boundary approach is computationally more efficient. The results of these simulations demonstrate that, contrary to popular opinion, continuous mappings such as the Gal-Chen and Somerville transformation are not inherently limited to gentle slopes. Calculations for a strongly stratified case are also presented to point out the substantial differences from the neutral boundary layer flows.
© 2007 Elsevier Inc. All rights reserved.

Keywords: Urban boundary layers; Terrain-following coordinates; Immersed-boundary approach; Flow past a building

1. Introduction

Recent world events have heightened society's awareness of its vulnerability to the release of chemical and biological agents either through intentional or inadvertent actions. Of particular concern is the release of these

* Corresponding author. Tel.: +1 303 497 8972; fax: +1 303 497 8181.
E-mail address: smolar@ucar.edu (P.K. Smolarkiewicz).

agents in heavily populated urban areas. Thus it becomes a matter of some urgency to be able to detect and forecast the transport and diffusion of hazardous substances in urban areas for effective evacuation and treatment strategies. However, modeling the flows in urban areas around many buildings of different sizes and shapes is an extremely complex problem which taxes the numerical simulation capabilities of both the meteorological and engineering communities. Current approaches to the problem are varied [1], from very simple Gaussian plume semi-empirical estimates through a hierarchy of CFD (computational fluid dynamics) models, with sophisticated large eddy simulations (LES) at the upper end. Recent LES by Liu et al. [2] and Cui et al. [3] are representative of computational studies of neutral planetary boundary layer (PBL) flows past idealized urban street canyons. Both works assume explicit internal boundaries to represent the buildings, while relying on finite-element [2] and finite-volume discretizations [3] of the governing equations.

In general, numerical modeling of natural urban flows is still in its infancy, and because of the tremendous computational burden involved in modeling realistic urban structures, it is important to carefully consider computational efficiency versus accuracy tradeoffs of candidate modeling approaches. In this paper we report on a systematic numerical study of neutrally stratified boundary layer flow over a single complex structure. A unique aspect of our report is a thorough comparison of the model results to independent measurements in a wind tunnel. The structure used is a scale model of the Pentagon building, but the results obtained carry over to other complex constructions which may be embedded in any neutrally stratified urban environment. An example of stratified flow is also included for comparison to the neutral wind tunnel case. The ultimate goal of this research is to develop and identify reliable tools for quantifying the air flow past urban structures under various meteorological conditions.

We conduct building-resolving LES using two distinct methods to represent the edifice. The first method employs the Gal-Chen and Somerville terrain-following coordinate transformation [4] – a standard vertical-coordinate transformation used in many mesoscale atmospheric simulations. In this method, the building is effectively treated as orography, with the resulting slopes truncated according to the adopted grid resolution. The second method uses the immersed boundary approach – originated by Peskin in the area of computational biomechanics [5,6] – in which fictitious body forces in the equations of motion are introduced to represent the internal boundaries; see [7] for a recent review. The particular technique employed here adapts the *feedback forcing* of Goldstein et al. [8], with implicit time discretization admitting rapid attenuation of the flow to stagnation (within the building structure) in $O(\delta t)$ time comparable to the time step δt of the model.

Both methods are implemented in the same hydrodynamical code EULAG[1] widely documented in the literature; cf. [12–15] for recent developments and reviews. The EULAG's underlying numerics are the NFT schemes[2] based on the MPDATA transport algorithms [19,18,20]. The solutions use two different methods for representing the building, but with identical numerics otherwise, and are compared to each other and to wind tunnel data collected for neutral stratification. Profiles of first- and second-order moments at various locations around the building are analyzed, subsequently leading to a synthetic assessment of the efficacy of the two methods. Both approaches show good agreement with the data, and both appear viable tools for LES of urban flows. However, for the case investigated here, the immersed boundary method seems to be slightly more accurate overall and is computationally three times more efficient due to less stringent stability requirements.

A particularly encouraging byproduct of our study is a demonstration that continuous mappings, such as the Gal-Chen and Somerville transformation, are not inherently limited to gentle slopes – an established belief in the geophysical CFD community – and can be quite effective in representing steep urban structures. We point out the technical details of our approach that appear different from those used in traditional atmospheric/oceanic codes, which may be responsible for our successful implementation of the terrain-following coordinates as the orographic slopes approach the vertical. These (details) include particulars of the formula-

---

[1] The name EULAG [9] alludes to the capability to solve the fluid equations in either an Eulerian (flux form [10]) or a Lagrangian (advective form [11]) framework.

[2] The term "nonoscillatory forward in time" was introduced in the late nineties [16,17] to label a class of second-order accurate two-time-level algorithms for fluids built on modern nonlinear advection techniques that suppress/reduce/control numerical oscillations characteristic of higher order linear schemes; NFT was meant to distinguish from classical centered in time and space linear methods; cf. [18,12] for reviews and discussions.

tion of the elliptic pressure equation, deriving pressure boundary conditions along curvilinear boundaries, and selection of a suitable solver as well as calculation of transformation coefficients by finite-differencing fundamental tensor identities (e.g. "geometric conservation law") rather than evaluating them numerically from the analytic formulae. Although the immersed boundary approach may simplify some of these aspects, it still requires powerful elliptic solvers, as the implicit integrals of the fictitious body forcing translate to abruptly changing coefficients in the elliptic pressure equation. These results have important implications for the use of terrain-following coordinate systems with steep orography common in many geophysical applications.

The remainder of the paper is organized as follows. In the next section, the theoretical formulation of the fluid dynamics model is outlined. The numerical approximations to the governing equations are discussed in Section 3, with some potentially important technical nuances explained in appendices. Design of the numerical experiments and the corresponding results are discussed in Section 4. Remarks in Section 5 conclude the paper.

2. Fluid model: theoretical formulation

The nonhydrostatic model EULAG used in this study has been thoroughly documented in the literature; for recent discussions see [13–15]. In general, EULAG admits several optional formulations of the equations of motion [21,14]. Here, we are concerned with small-scale boundary-layer flows, and thus adopt the classical incompressible Boussinesq approximation. Consequently, we invoke only a small portion of the model's capabilities, thereby simplifying the presentation as well as the computational procedures. The scope of this paper justifies a concise, operator-like symbolic description of the governing equations. Wherever the operator symbols refer to coefficient matrices, they merely indicate matrix operations but do not follow the formalism of matrix algebra to the letter – for a thorough mathematical exposition refer to [13–15].

EULAG's governing equations are formulated (and solved) in transformed time-dependent curvilinear coordinates

$$(\bar{t}, \bar{\mathbf{x}}) \equiv (t, \mathcal{F}(t, \mathbf{x})),$$ (1)

with the assumptions that the coordinates $(t, \mathbf{x})$ of the physical domain are orthogonal and stationary – in particular, Cartesian in this paper – and the transformed horizontal coordinates $(\bar{x}, \bar{y})$ are independent of the vertical coordinate z. Given the transformation in (1), the governing equations considered here, can be compactly written as follows

$$\overline{\nabla} \cdot (\rho^* \bar{\mathbf{v}}^s) = 0,$$ (2)

$$\frac{d\mathbf{v}}{d\bar{t}} = -\widetilde{\mathbf{G}}\overline{\nabla}\pi' - \mathbf{g}\frac{\theta'}{\theta_b} - \beta\mathbf{v} + \mathcal{D}_m(e, \overline{\nabla}\bar{\mathbf{v}}) - \alpha_m\mathbf{v}'$$ (3)

$$\frac{d\theta'}{d\bar{t}} = -\bar{\mathbf{v}}^s \cdot \overline{\nabla}\theta_e - \beta(\theta - \theta_B) + \mathcal{D}_h(e, \overline{\nabla}\theta) - \alpha_h\theta'$$ (4)

$$\frac{de}{d\bar{t}} = \mathcal{S}(e) - \beta e$$ (5)

where, because of the coordinate transformation, the physical and geometrical aspects are interdependent. Insofar as the physics are concerned: $\mathbf{v}$ denotes the *physical* (i.e., measurable) velocity vector; θ, ρ, and π refer to potential temperature, density, and a density-normalized pressure, respectively; and $\mathbf{g}$ is the acceleration of gravity (vector). The $\mathcal{D}$ terms appearing in the momentum and entropy equations (3) and (4) symbolize viscous dissipation of momentum and diffusion of heat via, respectively, divergence of turbulent stresses and heat fluxes, with corresponding eddy coefficients proportional to the square root of the "turbulent kinetic energy" e whose evolution in (5) symbolizes the standard prognostic "TKE" subgrid-scale model where all usual sinks and sources were combined in the $\mathcal{S}(e)$ term; cf. [17,22] for details. Primes denote deviations from the hydrostatically balanced ambient (i.e., environmental) state $\mathbf{v}_e$, θ_e, and the subscript b refers to the Boussinesq reference state. The relaxation terms with coefficients α and β (functions of the coordinates), appearing on the r.h.s. of (3)–(5), represent fictitious forces whose eventual role is to attenuate the solution to prescribed states within the body of the building (denoted by the subscript B: $\mathbf{v}_B \equiv 0$) and in the vicinity of the open boundaries

of the model, respectively. Notably, all relaxation and viscous terms in the momentum and entropy equations represent parameterizations justified by expediency and, ultimately, by comparison with data.

The geometry of the coordinates in (1) enters the governing equations as follows: in the mass continuity equation (2), $\rho^* \equiv \rho_b \overline{G}$ with $\overline{G}$ denoting the Jacobian of the coordinate transformation; whereas in the momentum equation (3), $\widetilde{\mathbf{G}} \sim (\partial \overline{\mathbf{x}}/\partial \mathbf{x})$ symbolizes the renormalized Jacobi matrix of the transformation coefficients; $\overline{\nabla} \cdot \equiv \partial/\partial \overline{\mathbf{x}} \cdot$, and the total derivative is given by $d/d\overline{t} \equiv \partial/\partial \overline{t} + \overline{\mathbf{v}}^* \cdot \overline{\nabla}$, where $\overline{\mathbf{v}}^* \equiv d\overline{\mathbf{x}}/d\overline{t} \equiv \dot{\overline{\mathbf{x}}}$ is the *contravariant velocity*. Appearing in the continuity (2) and entropy (4) equations is the *solenoidal velocity*

$$\overline{\mathbf{v}}^s \equiv \overline{\mathbf{v}}^* - \frac{\partial \overline{\mathbf{x}}}{\partial t}, \tag{6}$$

that follows [23] from the generic (tensor invariant) form of incompressible continuity equation

$$\overline{G}^{-1}\left(\frac{\partial \rho^*}{\partial \overline{t}} + \overline{\nabla} \cdot (\rho^* \overline{\mathbf{v}}^*)\right) \equiv 0. \tag{7}$$

The transformation

$$\overline{\mathbf{v}}^s = \widetilde{\mathbf{G}}^{\mathrm{T}} \mathbf{v}. \tag{8}$$

relates the solenoidal and physical velocities directly. For further details of the metric and transformation tensors as well as the formulation of the viscous and dissipative terms in the governing equations, the interested reader is referred to [15] and references therein.

Following [14], the general dependence of $\overline{z}$ on (x, y, z, t) in (1) collapses to a similarity transformation

$$\overline{z} = \mathcal{C}(\xi)$$
$$\xi = \xi(x, y, z, t) := H_0 \frac{z - z_s(x, y, t)}{H(x, y, t) - z_s(x, y, t)}, \tag{9}$$

where H and z_s are the upper and lower surface elevations, respectively, H_0 denotes the vertical extent of the transformed model domain, and the function $\mathcal{C}$ conveniently admits a class of vertically stretched coordinates. The transformation in (9) is a generalization of the classical terrain-following Gal-Chen and Somerville [4] transformation. It has the computational advantage of separability into one- and two-dimensional fields. In particular, the Jacobian of the transformation is given as

$$\overline{G} = \left(\frac{d\mathcal{C}}{d\xi} \frac{\partial \xi}{\partial z}\right)^{-1} \left(\frac{\partial \overline{x}}{\partial x} \frac{\partial \overline{y}}{\partial y} - \frac{\partial \overline{x}}{\partial y} \frac{\partial \overline{y}}{\partial x}\right)^{-1} \equiv \left(\frac{d\mathcal{C}}{d\xi}\right)^{-1} \overline{G}_0 \overline{G}_{xy}, \tag{10}$$

with

$$\overline{G}_0 \equiv \left(\frac{\partial \xi}{\partial z}\right)^{-1} = \frac{H(x, y, t) - z_s(x, y, t)}{H_0}. \tag{11}$$

Throughout this paper, $\overline{x} = x$, $\overline{y} = y$ and $\xi = \overline{z}$; thereby employing the identity transformation in the horizontal (viz. $\overline{G}_{xy} \equiv 1$). Furthermore, the upper boundary is stationary and flat (viz. $H \equiv H_0$), and there is no vertical stretching of the lower-boundary-fitted coordinate $\overline{z}$ (viz. $d\mathcal{C}/d\xi \equiv 1$). The lower boundary is also stationary but inhomogeneous, $z_s = z_s(x, y)$, thereby reducing (9) to the classical case, standard in many atmospheric/oceanic models. In spite of the resulting mathematical simplifications, the actual EULAG program accommodates (1) and (9) in their full generality. We retain the consistent notation for conciseness of forthcoming discussions and ease of connection to earlier works.

3. Numerical approximations

Given (7), each prognostic equation that forms the Boussinesq system (3)–(5) can be written in two equivalent forms, either as a Lagrangian evolution equation

$$\frac{d\psi}{d\overline{t}} = R, \tag{12}$$

or an Eulerian conservation law

$$\frac{\partial \rho^* \psi}{\partial t} + \overline{\nabla} \cdot (\rho^* \overline{v}^* \psi) = \rho^* R. \tag{13}$$

Here ψ symbolizes components of v as well as θ' or e, and R denotes the associated r.h.s.

We approximate either (13) or (12) to second-order accuracy in space and time using the nonoscillatory forward-in-time (NFT) approach – see [18,12] for reviews and discussions. The particular NFT algorithm employed here can be formally written as

$$\psi_i^{n+1} = LE_i(\tilde{\psi}) + 0.5\delta t R_i^{n+1} \equiv \hat{\psi}_i + 0.5\delta t R_i^{n+1}; \tag{14}$$

where ψ_i^{n+1} is the solution sought at the grid point $(\bar{t}^{n+1}, \bar{x}_i)$, $\tilde{\psi} \equiv \psi^n + 0.5\delta t R^n$, and LE denotes a two-time-level either advective semi-Lagrangian [11] or flux-form Eulerian [10] NFT transport operator, viz. advection scheme.[3] The calculations reported in this paper used exclusively the second-order-accurate, monotone (FCT) [24], flux-form scheme MPDATA, the technical details of which are widely described in the literature; see [19,18,20] and references therein. For the reader's convenience and clarity of the following discussion, we outline the functional form of MPDATA in Appendix A.

Subgrid-scale (SGS) forcings $\mathcal{D}_m$, $\mathcal{D}_h$ and S – in (3)–(5), respectively – included in R are evaluated explicitly and to first-order. This is justified because they enter the equations of motion only as a consequence of a sub-grid-scale turbulence model, already as $\sim \mathcal{O}(\delta x^2)$ corrections. Technically, this eliminates the need for predicting SGS^{n+1} in R^{n+1} on the r.h.s. of (14), as $SGS(\psi^{n+1}) = SGS(\psi^n) + \mathcal{O}(\delta t)$. Programming wise, the definition of the auxiliary field $\tilde{\psi}$ is expanded as $\tilde{\psi} \equiv \psi^n + 0.5\delta t(R_{\text{rsv}}^n + 2R_{\text{sgs}}^n)$, while accounting only for the resolved forcing R_{rsv} in R^{n+1} on the r.h.s. of (14); cf. Sections 3.5.4 and 4.2 in [18] for discussion. The explicit first-order evaluation of SGS forcings improves the efficacy of the calculations. When required however, it can be extended to a trapezoidal integration, employed for the resolved forcing R_{rsv}, by means of an outer iteration scheme [25].

The template algorithm (14) already incorporates the assumption that all prognostic variables are defined at the same grid points $\bar{x}_i$. This is important for the efficacy of the model; see [9] for a discussion. In EULAG we allow two grid configurations: the unstaggered A-grid, where all variables are defined at the same positions, and the staggered B-grid, where a pressure variable is staggered one-half grid interval in all directions with respect to the other variables [26]. In either case, advection and diffusion modules mimic a staggered C-grid with fluxes evaluated at fictitious cell-wall locations surrounding data points $\bar{x}_i$, cf. Appendix A; whereas partial derivatives $\partial/\partial \bar{x}$ composing the Nabla operator $\overline{\nabla}$ on the l.h.s. of (2) as well as in the pressure gradient and convective-derivative terms, respectively, on the r.h.s. of (3) and (4) are approximated with standard second-order-accurate finite-difference formulae. All calculations reported in this paper were performed on the A-grid.

Note that Eq. (14) represents a system implicit with respect to all resolved variables in (3) and (4), because the velocity components, pressure, and potential temperature are assumed to be unknown at $n+1$. For the physical velocity vector v, it can be written compactly as

$$v_i = \hat{v}_i - 0.5\delta t(\tilde{G}(\overline{\nabla}\pi'))_i + 0.5\delta t R_i(v, \hat{\theta}'), \tag{15}$$

where

$$R_i(v, \hat{\theta}') \equiv -(\beta v + \alpha_m(v - v_e))_i - g\frac{1}{\theta_0}\frac{\hat{\theta}'_i - 0.5\delta t((\tilde{G}^T v) \cdot \overline{\nabla}\theta_e)_i}{1 + 0.5\delta t(\beta + \alpha_h)_i}, \tag{16}$$

with

$$\hat{\theta}' \equiv \hat{\theta}' + 0.5\delta t \beta(\theta_B - \theta_e), \tag{17}$$

accounts for the implicit representation of the buoyancy and relaxation forcings via (4), and the superscript $n+1$ has been dropped as there is no ambiguity. On grids unstaggered with respect to all prognostic variables,

---

[3] The flux-form Eulerian transport operator LE invokes the multiplicative factor ρ^{*n}/ρ^{*n+1} to account for time variability of the generalized density ρ^* due to coordinate dependence on time, see [12] for discussion.

(15) can be inverted algebraically (viz. locally) to construct expressions for the solenoidal velocity components that are subsequently substituted into (2) to produce an elliptic equation for pressure

$$\left\{ \frac{\delta t}{\rho^*} \overline{\nabla} \cdot \rho^* \widetilde{\mathbf{G}}^{\mathrm{T}}[\hat{\mathbf{v}} - (\mathbf{I} - 0.5\delta t \widehat{\mathbf{R}})^{-1} \widetilde{\mathbf{G}}(\overline{\nabla}\pi'')] \right\}_i = 0, \tag{18}$$

where $\widetilde{\mathbf{G}}^{\mathrm{T}}[\hat{\mathbf{v}} - (\mathbf{I} - 0.5\delta t \widehat{\mathbf{R}})^{-1} \widetilde{\mathbf{G}}(\overline{\nabla}\pi'')] \equiv \bar{\mathbf{v}}^s$ defined in (6). In (18), $\hat{\mathbf{v}}$ combines all explicit parts on the r.h.s. of (15) – so, $\widehat{\mathbf{R}}$ denotes the resulting linear (homogeneous) operator acting on $\mathbf{v}$ – and $\pi'' \equiv 0.5\delta t \pi'$; cf. [13] for the complete development. Boundary conditions imposed on $\bar{\mathbf{v}}^s \cdot \mathbf{n}$, subject to the integrability condition $\int_{\partial\Omega} \rho^* \bar{\mathbf{v}}^s \cdot \mathbf{n} \mathrm{d}\sigma = 0$, imply the appropriate boundary conditions on π'' [13,14]; for additional particulars see Appendix B. The resulting boundary value problem is solved – with accuracy to a judiciously specified threshold $\|(\delta t/\rho^*)\overline{\nabla} \cdot \rho^* \bar{\mathbf{v}}^s\| < \varepsilon$, see [16] for a discussion – using a preconditioned generalized conjugate residual GCR algorithm [27–29], a nonsymmetric Krylov subspace solver akin to the popular generalized minimum residual GMRES scheme, [27,30]. Given the updated pressure, and hence the updated solenoidal velocity, the updated physical and contravariant velocity components are constructed from the solenoidal velocities using the transformations (8) and (6), respectively.

The detailed form of the transformation coefficients – i.e., the entries of $\widetilde{\mathbf{G}}$ appearing throughout (3), (8), and (18) – was given in [13–15]. Here we only emphasize that – in contrast to the majority of atmospheric/oceanic models using the Gal-Chen and Somerville transformation – we evaluate the coefficients by differentiating the Jacobians $\overline{G}_0$, defined in (11), rather than using direct differentiation of z_s; see section 2.2 in [14] for an exposition. This aims at satisfying the fundamental tensor identities [15,31] at the finite difference level. In our experience, this approach minimizes the production of spurious vorticity at the curvilinear boundaries and accelerates convergence of the elliptic solver.

4. Experimental setup

The wind tunnel experiment, Fig. 1, was conducted in the US EPA Meteorological Wind Tunnel at the Fluid Modeling Facility; the laboratory setup is highlighted in Fig. 2. It employs a 1:200 scale model of the building, with a large scale neutrally stratified ambient (free-stream) flow $\mathbf{v}_e = (U_0, 0, 0)$ where $U_0 \approx 4 \, \mathrm{m \, s^{-1}}$. With the characteristic length scale of the model $L = 2 \, \mathrm{m}$, this gives a Reynolds' number $Re \approx 5 \times 10^5$, only two orders of magnitude lower than for natural atmospheric boundary layer flows. The experimental
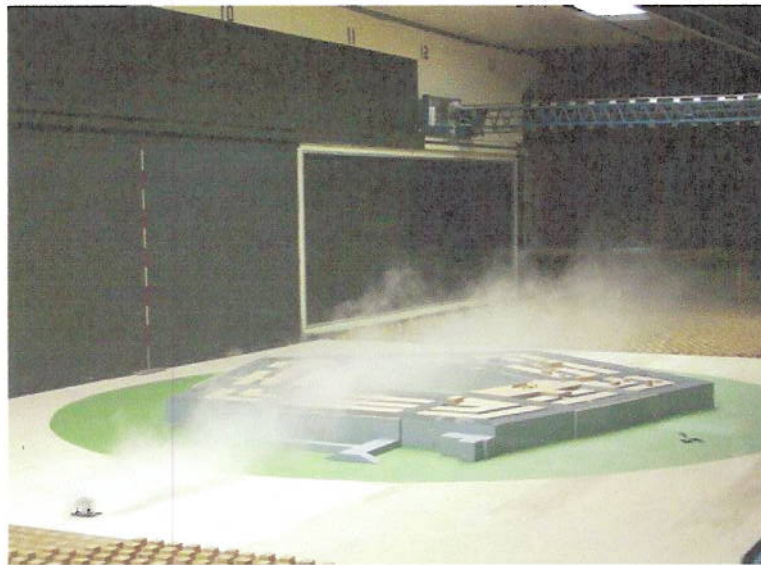

Fig. 1. Smoke visualization of point source plume around 1:200 scale model in the Meteorological Wind Tunnel.
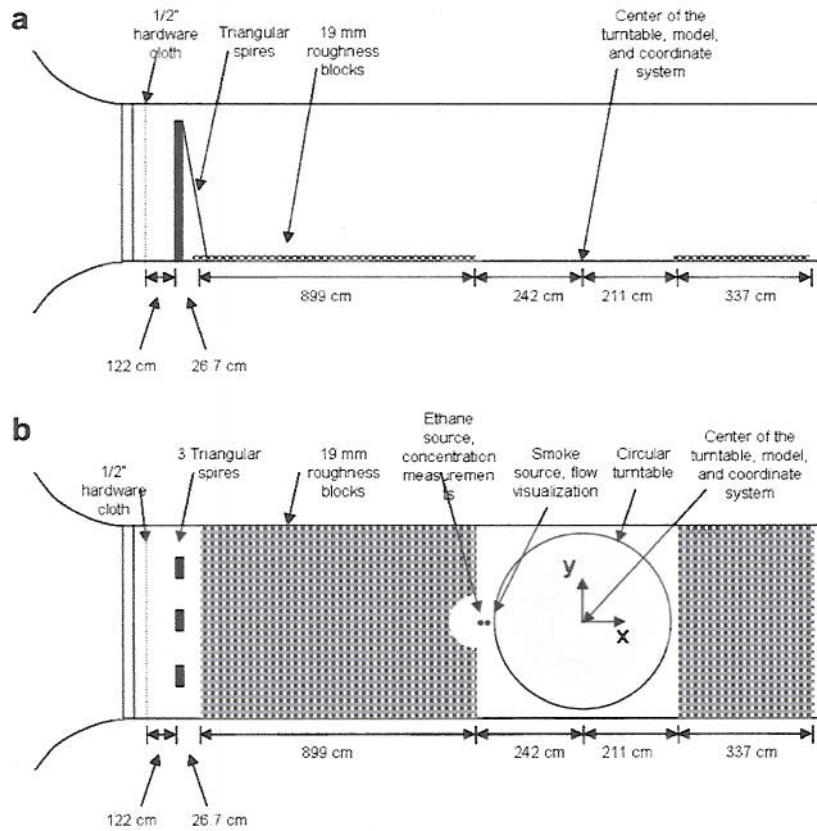
Fig. 2. Diagrammatic representation ((a) side view; and (b) plan view) of the wind tunnel setup. The hardware cloth indicates the origin of the test section. The domain of the test section is $18.38 \times 3.69 \times 2.12$ m^3, respectively, for length × width × height.

conditions exceed the critical Reynolds number required for a fully turbulent, Reynolds-number independent flow, thereby capturing all but the smallest scales of motion in a natural scenario [35].

Our numerical model setup mimics the aim of the wind-tunnel experiment by adopting the LES approach suitable for turbulent flows, but adds further idealizations for the sake of computational economy. The numerical representation of the model building with height $h = 0.1$ m is placed in the center of the $6.0 \times 3.7 \times 0.60$ m^3 domain – substantially shorter and lower than in the wind tunnel – covered with a uniform resolution of $\delta x = \delta y = \delta z = 0.01$ m, the highest practical at the time when the calculations were performed on 500 processors of an IBM BlueGene/L machine. Except for a few auxiliary sensitivity runs, the numerical simulations assume a flat test section and parameterize the upstream roughness blocks (Fig. 2) with the surface tangential stress proportional to the tangential flow times its norm, with a drag coefficient of $C_D = 0.1$. Similarly, the inflow boundary condition assumes laminar flow $[u_e(z), 0, 0]$ with $u_e(z) = u_0 + u_1 \ln(z) + u_2 \ln^2(z)$ fitted to the measured profile at the downwind edge of the upwind roughness blocks. Depending on the run, the time step $\delta t \in [0.00025, 0.001]$ s, with a total simulation time $T \in [1.2, 4.8]$ s, preceded with a model spin-up time over T_s, not necessarily equal to T. With $u_0 = 3.9$ m s^{-1}, the building length scale $L = 2$ m and the advective time scale $T_0 = L/u_0$, $T \in [2.3T_0, 9.4T_0]$. The spanwise lateral and the upper boundaries are assumed impermeable rigid lids, whereas open boundaries in the streamwise direction are mimicked with 0.20 m thick absorbing layers with inverse scales α_m in (3) growing linearly from zero at a distance 0.20 m away from the boundary to $(0.15 \text{ s})^{-1}$ at the boundary.

Fig. 3 shows the locations of profile data taken in the wind tunnel experiment with a laser-Doppler velocimeter (LDV). Note that measurements were taken not only upstream and in the wake, but also at various locations along the rooftop and in the recesses of the building. These recesses are very narrow, on the order of 6 δx, have a complex geometry, and are at various depths. Thus this single building provides a geometry as complex as many urban canyon settings.
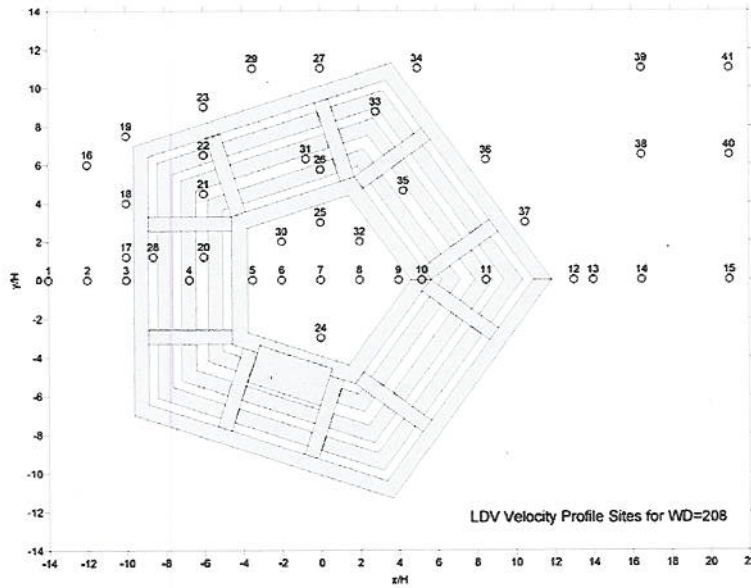
Fig. 3. LDV vertical profile locations for wind tunnel experiment.

Table 1
Specifications for the two reference runs

Approach	T_s (s)	T (s)	δt (s)	β^{-1}	N_p
IMB	2.4	4.8	1.00×10^{-3}	$0.5\delta t$	13.542×10^6
GCT	2.4	4.8	0.25×10^{-3}	∞	13.542×10^6

The first column identifies the approach, while the remaining columns list, respectively, the simulated spin-up time T_s, the total simulated time T for time mean and fluctuation segments, the time step δt employed, the time scale β^{-1} of the fictitious body forcing, and the total number of grid points N_p.

The numerical simulations are divided into two groups: runs employing the Gal-Chen and Somerville coordinate transformation, hereafter GCT, and calculations on a Cartesian mesh using the immersed-boundary approach, hereafter IMB. All calculations are performed at the maximum δt allowed by numerical stability criteria. For the GCT runs, this results in a time step 3–4 times smaller than that allowed in the IMB simulations. Each run has been conducted in 3 separate segments: a spin-up time to T_s, followed by time mean and fluctuation calculations over time T. Because in the wind tunnel vertical profiles of various time-averaged quantities were measured at 41 sites, Fig. 3, we chose to evaluate equivalent quantities at all grid points, for flexibility of post-processing. In the time-means segment, we start the flow calculations at T_s, and calculate in addition sums of selected fields over all time steps included in the segment, and store them to tape. In the fluctuation segment, we restart the flow calculations again at T_s and calculate variances of selected fields using the stored time-mean values. The averaging times in the wind tunnel experiment were ~120 s ($240T_0$), 24 times longer than the longest values of T used in the simulations ($9.6T_0$). Although our averaging times were dictated primarily by computational affordability, we note that those used in the laboratory – representative of a 7 h period under natural conditions – tend to favor the Reynolds-averaged Navier–Stokes' (RANS) approach. For the reader's convenience, Table 1 summarizes key aspects of the two reference runs; whereas further discussion of the immersed boundary scheme and the role of relevant time scales is included in Appendix C.

5. Results

Fig. 4 illustrates the IMB simulation of the flow; see [36] for an animation. It displays the instantaneous vertical velocity field w at $T = 4.8$ s in the central vertical xz plane and in the xy plane at $z = 0.5$ h – note the $3 \times$ exaggerated vertical scale in the xz cross-section. The corresponding GCT result is shown in Fig. 5.
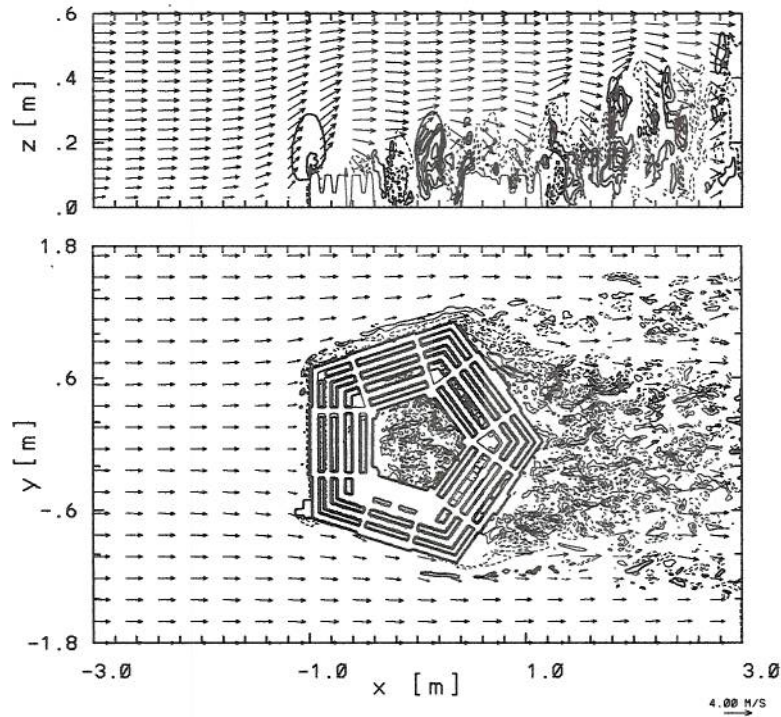
Fig. 4. Instantaneous IMB vertical velocity (w) field, with flow vectors superimposed, in the central vertical plane (upper panel) and in the horizontal plane at the half height of the building (lower panel). Isolines of w are plotted with a contour interval of $1/3$ m s^{-1}, dashed/solid lines represent negative/positive values and zero contour lines are not shown; the reference velocity vector in the lower right corner corresponds to 4 m s^{-1}.
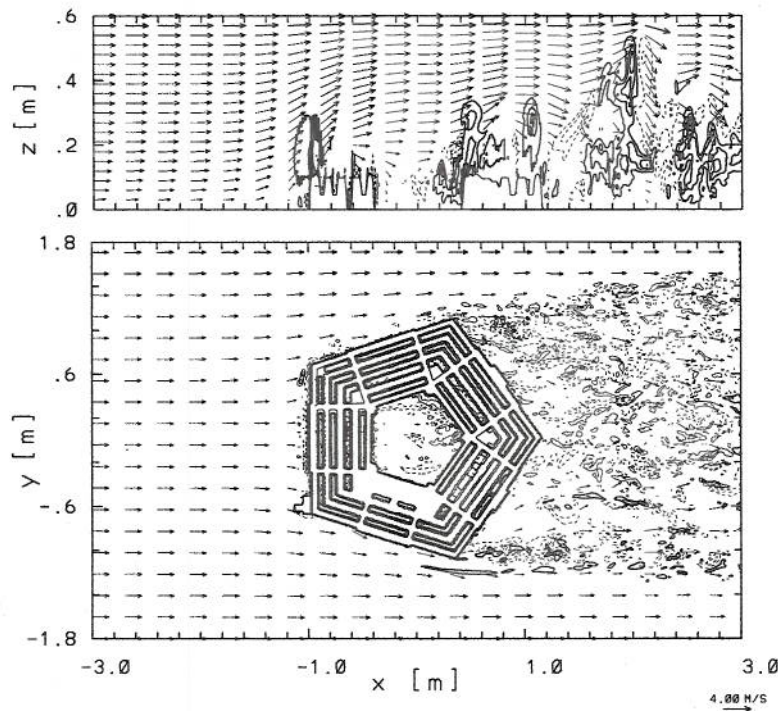
Fig. 5. As in Fig. 4 but for the GCT simulation.

Although both solutions seem qualitatively similar, there are some apparent differences. For instance, the IMB solution evinces more activity within the building courtyard and produces a more intense but narrower wake. Because the simulated flow is turbulent and intermittent – with the magnitude of the fluctuations comparable to that of the ambient flow – contrasting instantaneous results can be misleading. To better expose global differences between the IMB and GCT solutions, Fig. 6 juxtaposes the corresponding time-averaged $\langle w \rangle$ fields. Except for stronger updrafts/downdrafts at the flanks of the building in the IMB result, both results appear to match closely, and without reference to the measurements it seems impossible to judge which solution is more realistic.

The wind tunnel LDV measured vertical profiles include: profiles of the averaged velocity components $\langle u \rangle$, $\langle v \rangle$, $\langle w \rangle$; the component variances, e.g. $\langle u'u' \rangle \equiv \langle u - \langle u \rangle \rangle^2$ as well as their sum (0.5×, viz. the kinetic energy k' of velocity fluctuation); and two Reynolds' fluxes $\langle u'v' \rangle$ and $\langle u'w' \rangle$. With these nine profiles measured at 41 sites, cf. Fig. 3, a detailed comparison of the various runs with the data is not possible to present here. Below we summarize our overall experience with the simulation approaches, illustrated with selected results.

Tables 2–6 present the root mean square (RMS) error statistics for the measured first- and second-order normalized moment variables, derived by comparison to the wind tunnel LDV measurements for both the IMB and GCT methods at sites (cf. Fig. 3) representative of the following locations: 1 for upstream; 23 for lateral flanks; 7 for courtyard; 11 for rooftop; and 15 for wake. The calculated RMS error of the profile is
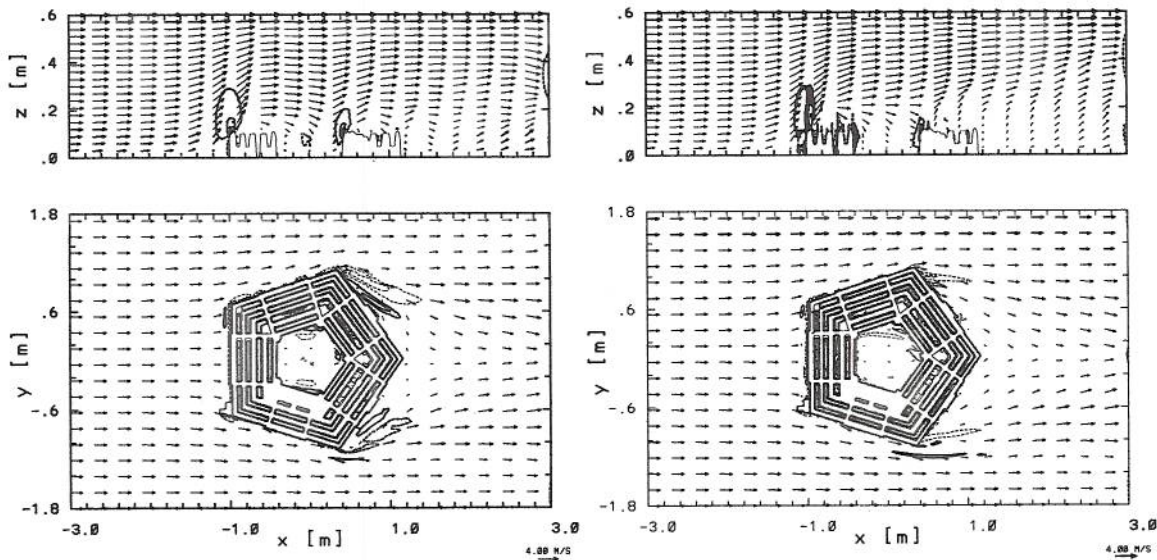

Fig. 6. Time-averaged vertical velocity fields $\langle w \rangle$ for IMB (left plates) and GCT (right plates); contour intervals and arrow lengths are the same as in Figs. 4 and 5.

Table 2
RMS error statistics of first- and second-order normalized moment variables for the IMB and GCT calculation methods compared to the normalized wind tunnel data (WAV and WMX for vertically averaged and maximal values) at site 1 upstream of the building

Src.	u	v	w	u'u'	v'v'	w'w'	k'k'	u'v'	u'w'
IMB	1.289	0.044	0.081	1.134	0.935	0.786	1.161	0.141	0.543
GCT	1.259	0.049	0.091	1.134	0.935	0.786	1.161	0.141	0.543
WAV	6.163	0.039	0.306	1.130	0.934	0.784	1.158	−0.013	−0.541
WMX	7.873	0.100	0.377	1.218	0.980	0.870	1.227	0.207	0.588

Square-roots of the magnitude of second-order moments are shown, for direct comparability with first-order fields; and all numerical entries are multiplied by 10, for compactness. See text for precise definitions.

Table 3
As in Table 2 but for site 23 on a lateral flank

Src.	u	v	w	$u'u'$	$v'v'$	$w'w'$	$k'k'$	$u'v'$	$u'w'$
IMB	1.032	0.301	0.440	1.066	0.922	0.748	1.123	0.331	0.515
GCT	0.978	0.131	0.355	1.042	0.922	0.747	1.115	0.331	0.515
WAV	6.795	0.388	0.481	1.093	0.923	0.748	1.138	0.323	−0.517
WMX	8.329	1.008	0.670	1.166	1.015	0.872	1.169	0.400	0.560

Table 4
As in Table 2 but for site 7 in the courtyard

Src.	u	v	w	$u'u'$	$v'v'$	$w'w'$	$k'k'$	$u'v'$	$u'w'$
IMB	0.855	0.124	0.262	0.844	0.829	0.729	0.872	0.349	0.671
GCT	1.631	0.257	0.153	1.385	0.931	0.786	1.467	0.419	0.660
WAV	4.723	0.052	−0.225	1.610	0.959	0.808	1.630	0.201	−0.595
WMX	8.266	0.160	0.414	1.962	1.046	0.931	1.946	0.258	0.773

Table 5
As in Table 2 but for site 10 at a rooftop

Src.	u	v	w	$u'u'$	$v'v'$	$w'w'$	$k'k'$	$u'v'$	$u'w'$
IMB	0.717	0.108	0.254	1.023	0.776	0.738	0.972	0.414	0.674
GCT	2.165	0.143	0.235	1.446	0.996	0.887	1.537	0.239	0.520
WAV	6.086	0.078	0.378	1.660	1.098	1.002	1.696	0.186	−0.702
WMX	8.193	0.244	0.881	2.034	1.358	1.285	2.119	0.330	0.928

Table 6
As in Table 2 but for site 15 in the wake of the building

Src.	u	v	w	$u'u'$	$v'v'$	$w'w'$	$k'k'$	$u'v'$	$u'w'$
IMB	0.471	0.122	0.291	0.739	0.580	0.275	0.597	0.305	0.249
GCT	1.515	0.102	0.323	1.017	0.723	0.762	1.033	0.354	0.728
WAV	4.680	0.058	0.238	1.367	1.152	1.054	1.466	0.139	−0.816
WMX	7.783	0.233	0.731	1.655	1.267	1.169	1.660	0.343	0.951

the average over the four grid points surrounding each site location at all vertical positions measured by the LDV. To avoid ambiguity, we write the adopted formulae explicitly. First we evaluate

$$\delta\xi = \sqrt{\frac{1}{N_v}\sum_{k=1}^{N_v}(\tilde{\xi} - \bar{\xi})^2} \tag{19}$$

where ξ refers to normalized measured profiles – e.g., $\langle u\rangle/U_0$ or $\langle u'w'\rangle/U_0^2$ – N_v is the number of vertical positions measured by the LDV (in general, different for each site), the tilde refers to the average over the 4 grid points surrounding each measurement, and the overbar denotes the measured profile. Next, for the second-order moments all numerical entries in the tables are transformed according to

$$\delta\xi^* = \mathrm{sgn}(\delta\xi)\sqrt{|\delta\xi|}, \tag{20}$$

to facilitate relating the magnitude of the fluctuations to the means. Finally, all numerical entries in the tables are premultiplied by the factor of ten, for the sake of compactness. The first column denotes the data source, either from calculations or measurements. Both WAV and WMX refer to wind tunnel measurements; denoting, respectively, the vertically averaged and maximal values of the profile. Together, the two characteristics aid in assessing "wiggliness" of fields with averages close to zero.
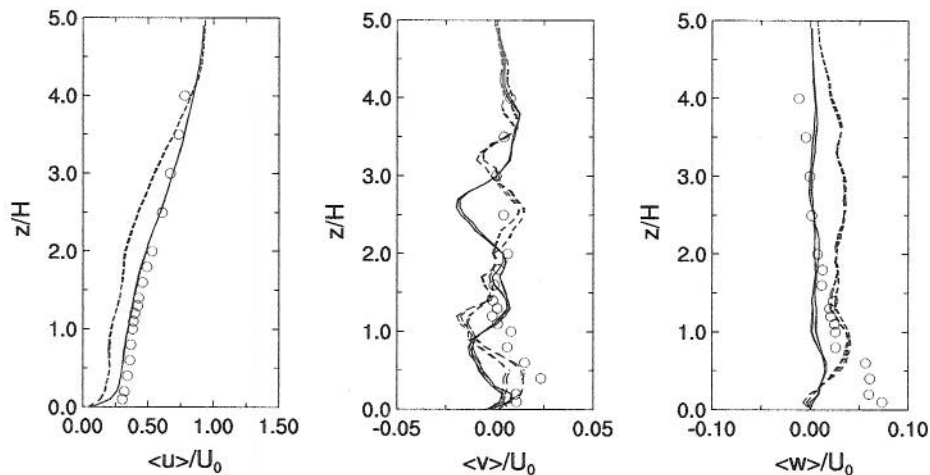
Fig. 7. Vertical profiles of mean velocity components in the building wake at site 15 (leeward most site at $x/H = 21$ and $y/H = 0$ in Fig. 3). Solid and dashed lines are for the IMB and GCT calculations, respectively, for the four grid points surrounding the LDV wind tunnel measurements (open circles).

As illustrated in the Tables, overall, the IMB technique provides slightly smaller RMS errors for most stations, but this trend is not universal and depends on the actual location and quantity being compared. In general, the mean profiles of the velocity components compare with measurements reasonably well for both IMB and GCT calculations. This is illustrated in Fig. 7 that displays the normalized mean profiles of $\langle u \rangle$, $\langle v \rangle$, and $\langle w \rangle$ at Site 15 (the leeward most site at $y = 0$ in Fig. 3). For the streamwise velocity component the IMB is more accurate up to $z = 3\,h$; whereas for the vertical velocity component, the IMB appears more accurate above $z = 2\,h$, while both simulations underpredict the measured weak updraft below about $z = 0.5\,h$. This is, however, not a global trend but only a local deviation, as at Site 12 (not shown) both calculations capture the low-level updrafts equally well, while overpredicting the vertical velocity at $z > 2\,h$.

Insofar as the fluctuation fields are concerned, both simulation techniques capture the magnitude and overall vertical structure of the measured profiles. For illustration, Fig. 8 shows, again for Site 15, profiles of velocity component variances, their sum ($0.5\times$), and the Reynolds fluxes. Although the IMB appears more accurate in some respects, there is no clear indication that it is uniformly superior to the GCT. Noteworthy, upwind of the building both simulations depart from the data to the same degree, predicting, in essence, no turbulent fluctuations. Since the amplitude of the measured fluctuations upwind of the building is roughly only twice smaller than in the lee, this cannot be attributed to wind tunnel noise. Our attempts to mimic the background wind-tunnel turbulence by introducing roughness blocks (cf. Figs. 1 and 2), allowing for adequate noise at the inflow boundary, or initializing subgrid-scale e with the $\langle k'k' \rangle$ profile measured at Site 1 (at the downwind edge of the upwind strip of roughness blocks) all failed to reproduce the measured fluctuation fields upwind of the building. We tend to believe that this is not due to an inadequacy of numerical model per se, but due to the unavailability of the actual initial and/or boundary conditions. Also, it should be remembered that the length of time averaging of the simulated fields is much less than in the wind tunnel. Based on our analysis of the experiments with shorter time averaging (not shown), longer time averages would provide closer agreement.

6. Strongly stratified flow regime

Although wind tunnel experiments of flow over blocks and other obstacles to represent buildings and street canyons are ongoing, e.g. [37,38], their utility is limited mainly to neutral stratification and unidirectional flow. Some stratified wind tunnel and towing tank measurements have been made, e.g. [39–41,43,42], but used simplified thermal structures and elementary obstacle shapes. These configurations may not always be representative of actual atmospheric flows in urban areas. For example, Frehlich et al. [44] using lidar profiling of the urban/suburban boundary layer in the Washington, DC area, show a wide variety of atmospheric conditions,
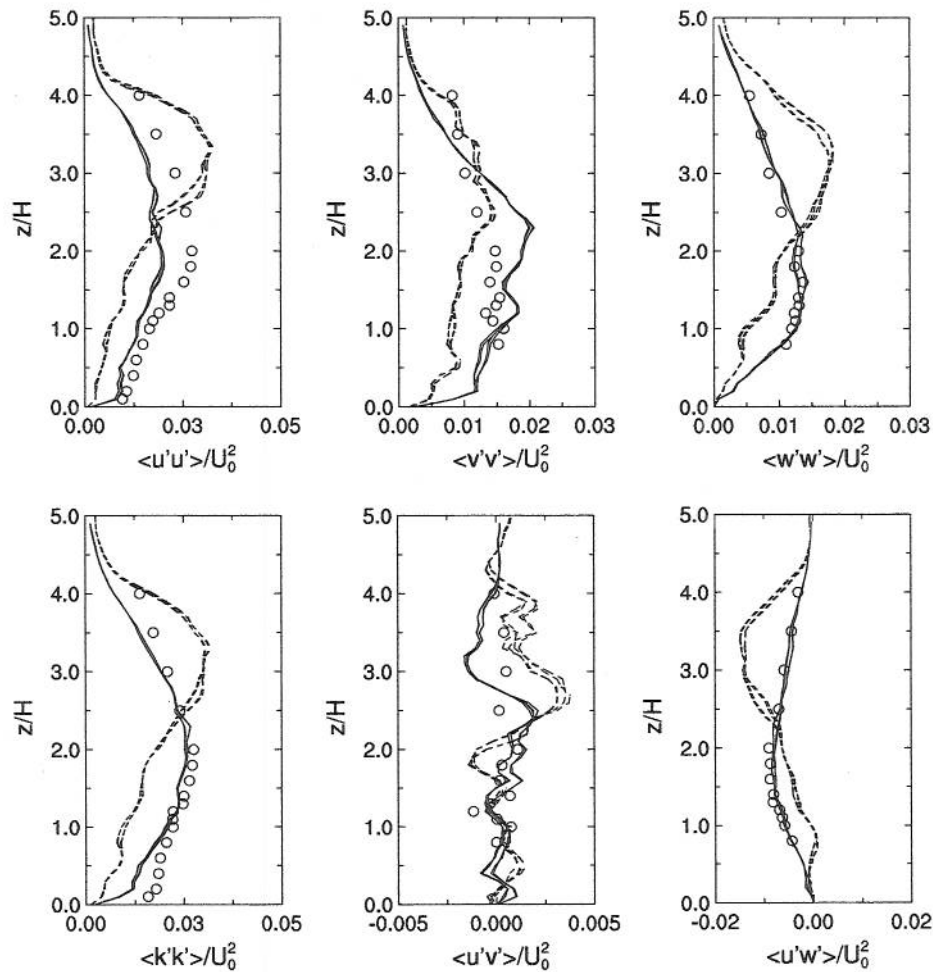
Fig. 8. As in Fig. 7 but for vertical profiles of the fluctuation fields.

from unstable convective conditions during the day to very stable conditions during night and early morning hours. Stable conditions are a particularly hazardous scenario since the inhibited mixing of contaminants implies higher and longer-lasting concentrations. Further, measurements are necessarily taken at only certain locations within the flow, and a fully three-dimensional quantitative assessment of the flow is difficult to achieve.

In this section we present a stably stratified case to compare and contrast to the neutral flow results given in the previous section. Although we do not have supporting data, the favorable comparisons obtained for the neutral case bolster our confidence in the integrity of the stably stratified results.

Elementary stratified flows with uniform ambient wind U_0 and buoyancy frequency N past obstacles of height h are characterized solely by the Froude number, $Fr \equiv U_0/Nh$ [45]. Of special interest is the fluid regime with $Fr \lesssim 0.5$, frequently referred to as low-Froude-number or strongly stratified flow. The distinguishing features of such flows include separation and flow reversal at lower levels in front of the obstacle, and the formation of intense vertically oriented vortices on the lee side of the obstacle [41,46,47]. Over the last two decades, low Froude number flows have attracted the considerable attention of the geophysical fluid dynamics community and have been the subject of numerous theoretical, observational, and modeling (both numerical and laboratory) studies; see [48] for a succinct review. Here, we include an example of low Froude number flow past the same pentagon-shaped building for two reasons. First, its distinguished features make it important for understanding/estimating contaminant dispersion past large buildings in weak nocturnal boundary layer

flows. Second, it is a numerically challenging extension of the neutral flow studies that further amplifies the utility of continuous mappings for representing urban structures in LES models.

In order to minimize departures from the neutral flow experiments discussed in preceding sections, we retain the original ambient wind profile and assume stably stratified ambient potential temperature $\theta_e(z)$ with a constant Brunt-Väisälä buoyancy frequency $N = \sqrt{g\theta_e^{-1}d\theta_e/dz} = 80$ s^{-1}. This (rescaled) buoyancy frequency N is three to four orders of magnitude larger than in natural atmospheric environments. This puts in question the validity and utility of standard SGS turbulence models like the one adopted in (5). To circumvent these potential difficulties, both the IMB and GCT simulations are performed in the implicit large-eddy-simulation (ILES) mode [49], relying solely on the numerical dissipation inherent in the nonoscillatory transport operator *LE* in (14). The implicit SGS property of our NFT approach has been widely discussed in the literature; see [17,12,50–52] and references therein. To further reduce disparities between the IMB and GCT simulations, the GCT run employs fictitious body forces with the attenuation time scale β^{-1} along the lower surface of the model $\bar{z} = 0$ where the orography $z_s > 0$.

With the large scale flow characterized by $U_0 = 4$ m s^{-1} and $N = 80$ s^{-1}, the dominant hydrostatic vertical wavelength $2\pi U_0/N = 0.1\pi$ m. In order to absorb both vertically and horizontally propagating gravity waves near the model boundaries, we increase the computational domain to $8.0 \times 3.7 \times 0.90$ m^3 (but keep the uniform resolution $\delta x = \delta y = \delta z = 0.01$ m) while expanding the thickness of the lateral absorbers to 0.60 m and adding an absorbing layer in the upper half of the domain. The inverse scales α_m in (3) for the lateral and vertical absorbers are, respectively, $(0.30 \text{ s})^{-1}$ and $(0.15 \text{ s})^{-1}$ at the corresponding boundaries. The time step is $\delta t = 0.001$ s for the IMB run, and $\delta t = 0.00025$ s for the GCT simulation. Both calculations are carried out over 4.8 s, after which time the flow has become well developed. Because of the overall expense of the GCT experiment, and lack of measurements for comparison, no subsequent runs were performed to calculate time-averaged or fluctuation fields.

Fig. 9 highlights the IMB (left column) and GCT (right column) instantaneous solutions at $T = 2.4$ s for the low Froude number flow. The upper row displays the vertical velocity field w in the central vertical xz plane. The lower row shows w in the xy plane at $z = 0.5$ h. Comparing these results with the corresponding results for neutral flow (Figs. 5 and 4) shows a completely different flow regime. The neutral boundary layer flows mainly
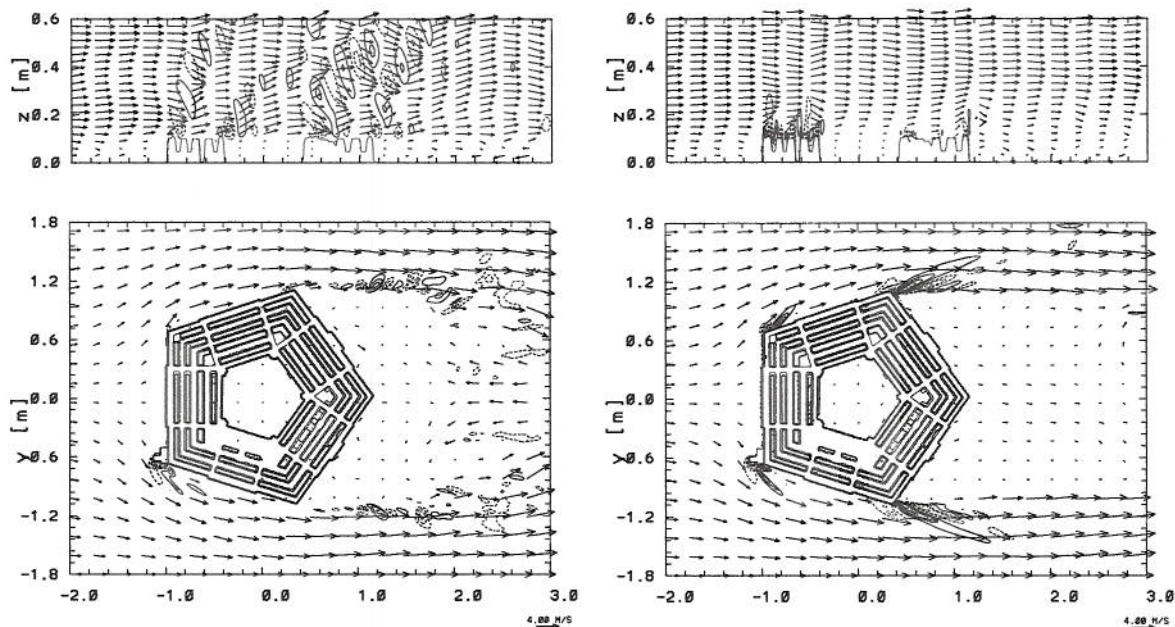

Fig. 9. Instantaneous vertical velocity w (the upper row) in the central vertical xz plane for IMB (left column) and GCT (right column) at $T = 2.4$ s. The lower row shows w in the xy plane at $z = 0.5h$. Contour intervals for w are 1/6 m s^{-1}, i.e., half of that in Figs. 4 and 5. The reference arrow length is 4 m s^{-1}, the same as in Figs. 4 and 5.

over the building and creates vigorous eddies in the wake; whereas the strongly stratified boundary layer flows mainly around the building and produces large scale vertically oriented vortices in the wake. In the latter case vertical motions are suppressed, taking the form of gravity wave fields generated by flow over the individual partitions of the building.

Although both the IMB and GCT calculations capture the salient features of the low Froude number flows, there are some noteworthy differences. In the IMB simulation the depth of lee eddies is slightly larger than 0.5 h – a value expected based on earlier works on low Fr number flows past smooth hills [41,46] – whereas it is slightly smaller than 0.5 h in the GCT run. While the flanks of the building shed fine scale eddies in the IMB experiment, they excite internal ship waves [53] in the GCT run. Furthermore, the wave field generated in the xz center plane of the GCT run appears evanescent with the waves excited predominantly by the fine scale building structures with a characteristic length scale $\sim$0.1 m, about three times shorter than the dominant vertical wavelength. In contrast, the IMB simulation produces vertically propagating gravity waves excited at the upwind and lee edges of primary building structure with the characteristic length scale $\sim$0.5 m. A close examination of the IMB results shows that vertical motions are suppressed in the recesses between individual corridors – a combined effect of relatively coarse resolution and a few grid intervals thick frictional boundary layer. In contrast, vertical motions within the recesses are evident in the GCT runs. Finally, as there are no grid points on the side walls in the GCT runs, frictional effects are suppressed there while spatial derivatives of z_s are underresolved (i.e., they enter the matrix of transformation coefficients $\widetilde{G}$ as narrow spike functions). Therefore, at least for this strongly stratified case, the flow in the recesses (equivalent to street canyons) from the IMB simulation appears to be underdeveloped, and would require higher horizontal resolution to match locally the GCT results. On the other hand, the wave field aloft in the GCT simulation appears to be too weak, and requires a smoother obstacle to match the IMB result.

To investigate the cause of these discrepancies further we performed an auxiliary experiment with the building replaced by an annulus with the inner and outer radius equal to 0.5 and 1 m, respectively, but with all flow parameters kept the same. Fig. 10 displays the results equivalent to those shown in Fig. 9, except that the annulus in the GCT run is smoothed with a double application of a standard 1-2-1 low-pass filter. The two solutions agree much better now. Interestingly, the frictional effects per se appear of lesser importance, as the identical GCT simulation but with the drag force either imposed only along the top of the annulus or turned off give a similar result.
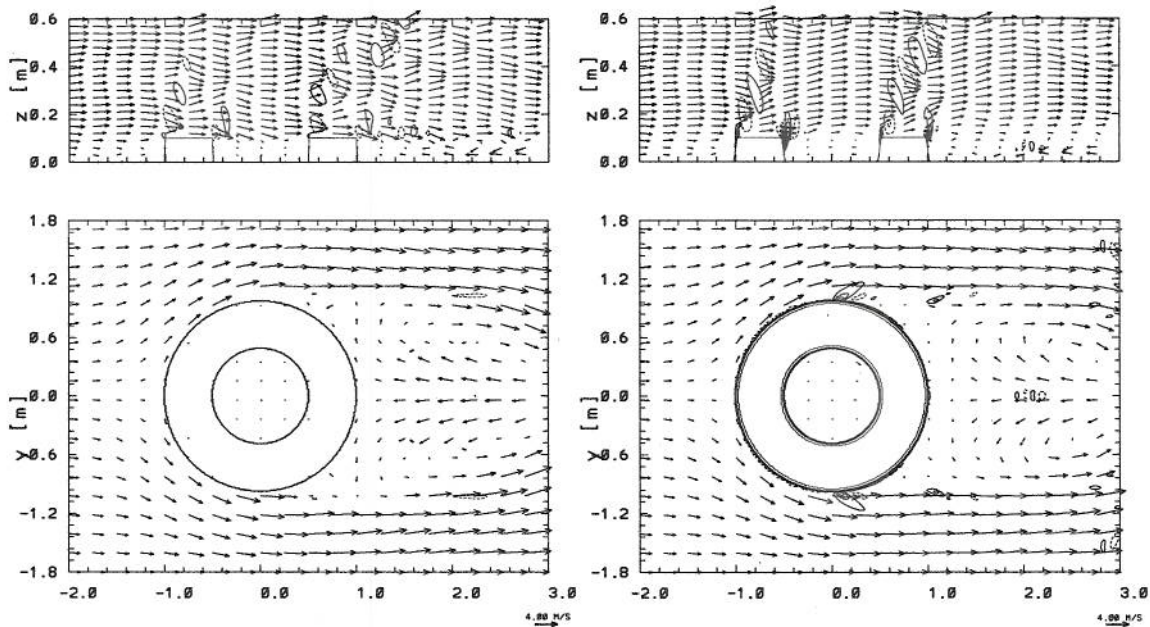

Fig. 10. As in Fig. 9 but for the annulus.

Having two solutions that differ in details, Fig. 9, it is only natural to ask which one is "correct". Without further measurements, or reference calculations with substantially finer effective resolution – e.g. by means of the NFT approach using an unstructured mesh [54,55] – we can only speculate that the correct result may fall somewhere in-between. The IMB integrations appear to overemphasize the frictional boundary layer effects, whereas the GCT calculations tend to underresolve building slopes, thus misrepresenting the long-wave portion in the power spectrum of gravity wave forcing. Although the IMB better captures the virtual microscale wind tunnel problem at hand, in the LES of natural stably stratified urban boundary layers a straightforward application of the IMB approach with a Cartesian mesh would likely overpredict the thickness of the frictional boundary layer, thereby making the equivalent GCT simulation with a partial-slip boundary condition preferable for its accuracy. On the other hand, the large-scale comparability of the two results and the quadruple computational cost of the GCT simulation still makes the IMB technique an attractive tool for computational studies.

7. Concluding remarks

We described a series of numerical experiments using a representative nonhydrostatic atmospheric model, with the aim to assess the efficacy of large scale computations for simulating natural urban boundary layer flows. The preexisting wind tunnel measurements of neutral flow past an elaborate scale model of the Pentagon building offer a rare opportunity to validate the predictive ability of numerical approximations to capture the statistical nature of atmospheric flows past complex structures. Here, we compared two distinct approaches: use of the classical terrain-following coordinate transformation of Gal-Chen and Somerville [4] (GCT) common in meteorological models; and an immersed-boundary approach (IMB), proven in many areas of computational fluid dynamics [7], in which fictitious body forces mimic the presence of complex obstacles embedded in a regular Cartesian grid. The common denominator of the two methods is their relative simplicity in circumventing the imposition of an explicit internal-boundary condition for elliptic problems in incompressible-type fluid models. The comparison of the two methods against the wind tunnel measurements shows that both provide sound results but the IMB technique is more efficient due to its less stringent computational stability requirements.

Although we judge the outcome of this study encouraging, we recognize that extrapolation of our results to natural scenarios should proceed with caution. Notably, our straightforward IMB employs effectively no-slip boundary conditions at the building walls, whereas the GCT is more flexible in admitting partial-slip drag laws. In contemporary meteorological LES models posed on structured grids, the IMB will tend to overpredict the thickness of frictional boundary layers, thus effectively smoothing the obstacle structure and obscuring the flow details in street canyons. More sophisticated IMB schemes can be designed, but at the price of loosing the simplicity of the approach. The problem gets even further complicated for thermally stratified flows, where the IMB offers little flexibility with boundary conditions for heat transfer. Consequently, we speculate that in many natural flow applications the GCT approach will offer superior accuracy, thereby offsetting the benefits of IMB's lower computational cost. Notwithstanding, the simplicity of the latter allows for easy implementation in standard atmospheric models, thus offering a choice of methods as well as their hybridization for representing urban structures in complex terrain.

An important byproduct of this study – urban flows aside – is a demonstration that continuous mappings, such as the Gal-Chen and Somerville transformation, are not inherently limited to gentle slopes. An established belief in the atmospheric CFD community is that the terrain-following coordinate transformation fails above certain slopes (circa ten, or a few tens of degrees depending on the source of information). Here we performed calculations with slopes exceeding 80°, and demonstrated their soundness. Inasmuch as we are not in a position to comment why continuous mappings fail in other applications, we commented on the numerical particulars of our approach (and referred the interested reader to earlier publications for more technical details) that may be responsible for the success of our implementation. These particulars include formulation of the elliptic pressure equation (18), deriving pressure boundary conditions along curvilinear boundaries (Appendix B) together with selecting a suitable nonsymmetric solver [27–29], and calculation of the transformation coefficients by exploiting the fundamental tensor identities [14,15,31]. We hope this information will assist the reader interested in using terrain-following coordinate systems to represent steep orography in computational model for atmospheric/oceanic flows.

The technical ability of handling increasingly steep slopes raises an interesting question at the very roots of numerical analysis: "what happens as the grid resolution tends to zero?" Clearly, there can be no convergence in the standard functional sense, as the coordinate transformation (9) becomes problematic in the vertical-wall limit. A formalist might argue that the model solution space is not complete, because for any fixed and sufficiently smooth obstacle-shape the solutions must converge as implied by the underlying control-volume numerics; e.g. at the second-order rate as the flow becomes laminar.[4] However, for the class of high-Reynolds number flows discussed in this paper, the formal convergence is a moot issue, as the affordable resolution is still far from that limit and the only convergence one may demand from LES is for the statistics.[5] The grid-spacing of 0.01 m appears to resolve well the larger scales of the forcing – note little variability of the average profiles in points surrounding the measurement site in Figs. 7 and 8, and their reasonable comparability for different methods of representing the edifice – but it is marginal, or even turns out to be inadequate, where small scales do not average out from statistics (cf. Fig. 9). Because we are not aware of any relevant alternate results available for further comparison, we investigate the strengths, weaknesses and avenues for improvement of the advocated methods in a separate study [56], using simple building shapes and flow scenarios documented in the literature. The summary of our findings will be reported in future publications.

Acknowledgments

Appendix A. MPDATA

In its basic form, MPDATA is sign preserving, fully second-order accurate, and conservative. A variety of options have been documented that extend MPDATA to full monotonicity preservation, to third-order accuracy, and to fields that do not preserve sign (such as momentum). Unlike most nonoscillatory methods, MPDATA is based directly on the *convexity* of upwind advection – i.e., the numerical solutions remain bounded by surrounding local values from the preceding time step, given a uniform advecting flow and adequately limited temporal increment; for nonuniform flow a weaker condition of sign preservation can be assured – rather than on the idea of flux limiting. In practical terms, the algorithm consists of a series of donor cell steps; the first step provides a first-order accurate solution while subsequent steps compensate higher-order truncation errors, derived analytically from a modified-equation analysis of the upwind scheme. To illustrate, an elementary M-dimensional advection problem $\partial\psi/\partial t + \nabla\cdot(\psi\mathbf{v}) = 0$ – where ψ is a scalar field advected with an arbitrary flow $\mathbf{v}$ – yields the MPDATA solution [18] written compactly on a regular grid as

$$\psi_{\mathbf{i}}^{(k)} = \psi_{\mathbf{i}}^{(k-1)} - \sum_{I=1}^{M} \left[F\left(\psi_{\mathbf{i}}^{(k-1)}, \psi_{\mathbf{i}+\mathbf{e}_I}^{(k-1)}, V_{\mathbf{i}+1/2\mathbf{e}_I}^{I(k)}\right) - F\left(\psi_{\mathbf{i}-\mathbf{e}_I}^{(k-1)}, \psi_{\mathbf{i}}^{(k-1)}, V_{\mathbf{i}-1/2\mathbf{e}_I}^{I(k)}\right) \right],$$

where: $\mathbf{i} \equiv (i^1, \ldots, i^M)$ denotes a location on the grid; $\mathbf{e}_I$ is the unit vector in the Ith of M spatial directions; F is the donor-cell flux function that takes the value of either the first or second argument depending on the sign of the normalized advective pseudo velocity V^I in Ith direction; integer and half integer indices correspond to the cell centers and edges respectively; and $k = 1, \ldots, \text{IORD}$ numbers the MPDATA iterations such that

---

[4] For a demonstration see [55] where an MPDATA-based NFT approach has been employed for integrating compressible Euler equations on unstructured meshes.

[5] For a demonstration of the LES convergence of the EULAG's results see [50].

$$\psi^{(0)} \equiv \psi^n; \quad \psi^{(\text{IORD})} \equiv \psi^{n+1}$$

$$V^{I(k+1)} = V^I(\mathbf{V}^{(k)}, \psi^{(k)}, \nabla \psi^{(k)}); \quad V^{I(1)}_{i+1/2\mathbf{e}_I} \equiv v^I|^{n+1/2}_{i+1/2\mathbf{e}_I} \frac{\delta t}{\delta x^I}.$$

Here, n and $n+1$ denote temporal levels $t^{n+1} = t^n + \delta t$, and δx^I denotes spatial grid increment in the Ith direction.

Appendix B. Pressure boundary conditions

Because curvilinear boundaries are notorious for inhibiting the convergence of Krylov-subspace methods [32], careful design of the discretized boundary conditions may dictate the overall model performance. Our approach in EULAG exploits the regularity of the boundary-fitted coordinate transformation (9) at the very heart of the GCR solver. Below we highlight the essential steps that may be useful for other model designs.

Consider first an archetype iteration for the elliptic problem in (18)

$$\phi^{k+1} = \phi^k + b^k r^k, \tag{21}$$

where, ϕ is a shorthand for $\pi''|_\mathbf{i}$, k numbers the iterations, b is a coefficient (constant at any given k), and r denotes the residual error, i.e., the actual value of the l.h.s. of (18) for $\pi''|^k$. For either Dirichlet or Neumann boundaries, the recurrence relation (21) implies, respectively,

$$\phi_\mathrm{B}^{k+1} = \phi_\mathrm{B}^k + b^k r_\mathrm{B}^k, \tag{22}$$

$$\mathbf{n} \cdot \mathbf{Grad}\, \phi^{k+1}|_\mathrm{B} = \mathbf{n} \cdot \mathbf{Grad}\phi^k|_\mathrm{B} + b^k \mathbf{n} \cdot \mathbf{Grad}\, r^k|_\mathrm{B}, \tag{23}$$

where subscript B refers to the boundary values, and the Ith component

$$\mathbf{Grad}^I = \sum_{J=1,3} C^{IJ} \frac{\partial}{\partial \bar{x}^J}, \tag{24}$$

with coefficients C^{IJ} depending on all the coordinates; see Appendix A in [13] for a complete development. Eq. (24) refers to the operator manipulations in (18) – as the latter may be thought loosely of as $\mathbf{Div} \cdot \bar{\mathbf{v}}^s = 0$ with

$$\bar{\mathbf{v}}^s = \check{\mathbf{v}} - \mathbf{Grad}\, \phi, \tag{25}$$

where $\check{\mathbf{v}}$ symbolizes the explicit part. The recurrences (22) or (23) imply that if the boundary conditions were satisfied at the preceding iteration, they will be satisfied at the subsequent iteration, given that the boundary conditions on r or $\mathbf{Grad}\, r$ are homogeneous. Thus, to ensure the correct boundary conditions throughout the iteration process, it is important to satisfy them from the outset – i.e., at the initialization of the iteration loop, and to maintain the equivalent homogeneous boundary conditions while computing directional vectors, residual errors, and solution-error estimates that enter advanced Krylov-subspace solvers; see [33,34] for tutorials. In particular, noting that the Dirichlet boundary conditions for normal solenoidal velocities $\mathbf{n} \cdot \bar{\mathbf{v}}_\mathrm{B}^s = V_\mathrm{B}$ [14] imply Neumann conditions for pressure

$$\mathbf{n} \cdot \mathbf{Grad}\, \phi|_\mathrm{B} = \mathbf{n} \cdot \check{\mathbf{v}} - V_\mathrm{B} \tag{26}$$

one can express the boundary pressure gradient term in (25) with (26), thereby assuring that the correct boundary conditions are applied at the initialization of the iteration loop. In the iterations that follow, the corresponding gradient term of the residual error, directional vectors, etc., must be set to zero.

On general curvilinear grids implementing (26) may be cumbersome, because each velocity component in (25) shares all three partial spatial derivatives. We note, however, that among nine coefficients C^{IJ}, the diagonal entries C^{II} never vanish regardless of the complexity of the mapping in (1). Consequently, at solver initialization, we evaluate all partial derivatives explicitly from the pressure field available on the grid – e.g. from the previous time step of the model – *except* for the "diagonal" partial derivatives at the model boundaries; e.g. $\partial \phi / \partial \bar{z}$ at $\bar{z} = 0, H_0$, or $\partial \phi / \partial \bar{x}$ at $\bar{x} = 0, LX$. The diagonal boundary derivatives are computed from (26) with the explicit off-diagonal terms, and are implemented consistently in all three components of (25). At the domain edges there are two diagonal derivatives available, while all three derivatives are diagonal at the

domain corners. Within the iteration loop, we do the same for the residual error, directional vectors, or solution error estimate: at the boundaries, the diagonal derivatives are computed from the homogeneous boundary conditions, while all the others from the preceding iteration. Formally, this is equivalent to admitting within r^k on the r.h.s. of (21) the diagonal partial derivatives at the boundaries taken at $k+1$, i.e., implicit.

Appendix C. Immersed-boundary scheme; further details

Here, we motivate our choice of the particular form of the fictitious body forcing in governing Eqs. (3)–(5) and of the inverse time scale β used in calculations summarized in Table 1.

Consider the integral form of an elementary ODE describing a forced damped harmonic oscillator

$$\frac{d\psi}{dt} = -\gamma \int_0^t \psi \, d\tau - \beta\psi + A\sin(\omega t), \tag{27}$$

an archetype for many immersed boundary schemes [8]. For consistency with the NFT fluid model algorithm (14), we assume Crank–Nicholson time discretization of (27)

$$\psi^{n+1} = \hat{\psi} + 0.5\,\delta t R^{n+1}; \hat{\psi} \equiv \psi^n + 0.5\,\delta t R^n \tag{28}$$

where

$$R^n = -\gamma \mathcal{I}^n(\psi) - \beta\psi^n + A\sin(\omega t^n); \quad \mathcal{I}^n(\psi) \equiv \delta t \sum_{k=1}^n 0.5(\psi^{k-1} + \psi^k) \tag{29}$$

Noting that $\mathcal{I}^{n+1}(\psi) = \mathcal{I}^n(\psi) + 0.5\delta t(\psi^n + \psi^{n+1})$, (28) can be rewritten as

$$\psi^{n+1} = \hat{\hat{\psi}} - 0.5\delta t(\beta + 0.5\delta t\gamma)\psi^{n+1} \tag{30}$$

with the explicit part $\hat{\hat{\psi}} = \hat{\psi} + 0.5\delta t[A\sin(\omega t^{n+1}) - \gamma(\mathcal{I}^n(\psi) + 0.5\delta t\psi^n)]$. Because $\hat{\hat{\psi}}$ does not depend on ψ^{n+1}, the closed-form trapezoidal integral of (27) takes the compact form

$$\psi^{n+1} = \hat{\hat{\psi}}/[1 + 0.5\,\delta t(\beta + 0.5\,\delta t\gamma)] \tag{31}$$

Instead of programming an immersed-boundary scheme with arbitrary γ and β into the fluid code, we employed our archetype model "off line", to test the benefits of various choices of γ and β. With the goal of damping the flow to stagnation (within the body of building) in $\mathcal{O}(\delta t)$, we considered $\beta^{-1} \sim \mathcal{O}(\delta t)$; see Fig. 11 for an illustration. Within this range we found the solution behavior insensitive to the choice of γ. Consequently, in the EULAG code we neglect the integral term in (27), thus assuming $\gamma \equiv 0$.

With $\gamma \equiv 0$, (31) can be written explicitly as

$$\psi^{n+1} = \frac{\psi^n(1 - 0.5\,\delta t\beta) + \delta t A\cos(\omega\delta t/2)\sin(\omega t^{n+1/2})}{1 + 0.5\,\delta t\beta} \tag{32}$$
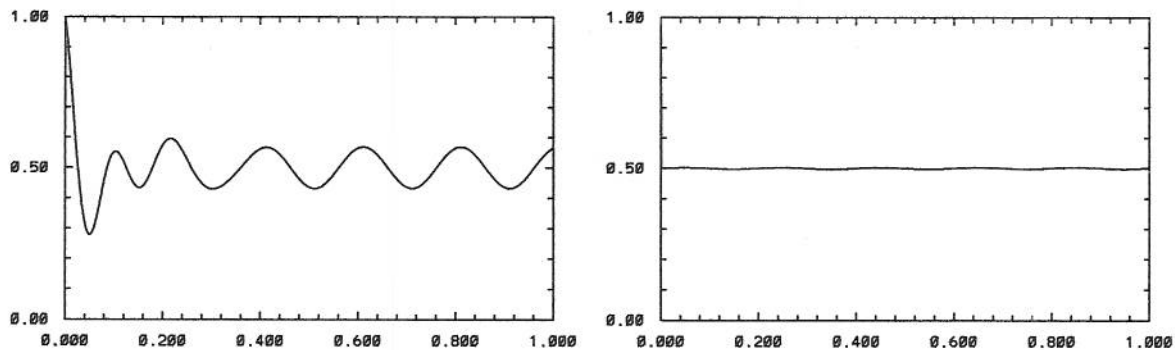

Fig. 11. Example of integrating (27) with an implicit second-order-accurate scheme (31). Here, $\delta t = 1/1000$, $\gamma = 2\pi/(2\delta t)$, $\omega = 2\pi/(200\delta t)$, $A = 1/(200\delta t)$, $\psi(t=0) = 1$, and $\beta^{-1} = 40\delta t$ (left plate) or $\beta^{-1} = 0.5\delta t$ (right plate); t and ψ are the abscissa and ordinate, respectively.

In the absence of external forcing, $A \equiv 0$, and $\beta^{-1} = 0.5\,\delta t$ damps the solution to zero within a single time step; shorter time scales give stable but oscillatory solutions. In general, for non-trivial external forcings there may be a conflict between the two terms in (32). While the first term favors $\beta^{-1} \gtrsim 0.5\,\delta t$, the contribution from the second term diminishes rapidly as $\beta^{-1} \to 0$; in such a case, a variable in time β may be preferred. In the application at hand, however, the primary external forcing is the pressure gradient that responds instantaneously to flow departures from solenoidal. In addition to the large scale components reflecting overall flow development, in turbulent flows it can have a rapidly oscillating component that reflects local small-scale adjustments. In (32), the large scale components correspond to $A = \psi_0/T$ and $\omega = 2\pi/T$ with $T \gg \delta t$, whereas the rapidly oscillating part corresponds to $A \sim \mathcal{O}(\psi_0/\delta t)$ and $\omega \leqslant 2\delta t$. In both cases setting $\beta^{-1} = 0.5\,\delta t$ is effective, as illustrated by the simple archetype model and verified by LES in Section 5.

Appendix D. Supplementary data

Supplementary data associated with this article can be found, in the online version, at doi:10.1016/j.jcp.2007.08.005.

References

[1] 9th Annual George Mason University Conference on Atmospheric Transport and Dispersion Modeling. http://camp.gmu.edu/9th-announcement.html.

[2] C.-H. Liu, M.C. Barth, D.Y.C. Leung, Large-eddy simulation of flow and pollutant transport in street canyons of different building-height-to-street-width ratios, J. Appl. Meteor. 43 (2004) 1410–1424.

[3] Z. Cui, X. Cai, C.J. Baker, Large-eddy simulation of turbulent flow in a street canyon, Q. J. Roy. Meteor. Soc. 130 (2004) 1373–1394.

[4] T. Gal-Chen, C.J. Somerville, On the use of a coordinate transformation for the solution of the Navier–Stokes equations, J. Comput. Phys. 17 (1975) 209–228.

[5] C.S. Peskin, Flow patterns around heart valves: a numerical method, J. Comput. Phys. 10 (1972) 252–271.

[6] C.S. Peskin, Numerical analysis of blood flow in the heart, J. Comput. Phys. 25 (1977) 220–252.

[7] R. Mittal, G. Iaccarino, Immersed boundary methods, Ann. Rev. Fluid Mech. 37 (2005) 239–261.

[8] D. Goldstein, R. Handler, L. Sirovich, Modeling a no-slip flow boundary with an external force field, J. Comput. Phys. 105 (1993) 354–366.

[9] P.K. Smolarkiewicz, L.G. Margolin, On forward-in-time differencing for fluids: an Eulerian/semi-Lagrangian nonhydrostatic model for stratified flows, Atmosphere-Ocean 35 (1997) 127–152.

[10] P.K. Smolarkiewicz, L.G. Margolin, On forward-in-time differencing for fluids: extension to a curvilinear framework, Monthly Weather Rev. 121 (1993) 1847–1859.

[11] P.K. Smolarkiewicz, J.A. Pudykiewicz, A class of semi-Lagrangian approximations for fluids, J. Atmos. Sci. 49 (1992) 2082–2096.

[12] P.K. Smolarkiewicz, J.M. Prusa, Forward-in-time differencing for fluids: simulation of geophysical turbulence, in: D. Drikakis, B.J. Guertz (Eds.), Turbulent Flow Computation, Kluwer Academic Publishers, Dordrecht, 2002, pp. 279–312.

[13] J.M. Prusa, P.K. Smolarkiewicz, An all-scale anelastic model for geophysical flows: dynamic grid deformation, J. Comput. Phys. 190 (2003) 601–622.

[14] N.P. Wedi, P.K. Smolarkiewicz, Extending Gal-Chen and Somerville terrain-following coordinate transformation on time dependent curvilinear boundaries, J. Comput. Phys. 193 (2004) 1–20.

[15] P.K. Smolarkiewicz, J.M. Prusa, Towards mesh adaptivity for geophysical turbulence, Int. J. Numer. Method Fluids 47 (2005) 789–801.

[16] P.K. Smolarkiewicz, V. Grubišić, L.G. Margolin, On forward-in-time differencing for fluids: stopping criteria for iterative solutions of anelastic pressure equations, Monthly Weather Rev. 125 (1997) 647–654.

[17] L.G. Margolin, P.K. Smolarkiewicz, Z. Sorbjan, Large-eddy simulations of convective boundary layers using nonoscillatory differencing, Physica D 133 (1999) 390–397.

[18] P.K. Smolarkiewicz, L.G. Margolin, MPDATA: a finite difference solver for geophysical flows, J. Comput. Phys. 140 (1998) 459–480.

[19] P.K. Smolarkiewicz, A fully multidimensional positive definite advection transport algorithm with small implicit diffusion, J. Comput. Phys. 54 (1984) 325–362.

[20] P.K. Smolarkiewicz, Multidimensional positive definite advection transport algorithm: an overview, Int. J. Numer. Methods Fluids. 50 (2006) 1123–1144.

[21] P.K. Smolarkiewicz, L.G. Margolin, A.A. Wyszogrodzki, A class of nonhydrostatic global models, J. Atmos. Sci. 58 (2001) 349–364.

[22] U. Schumann, Subgrid length-scales for large-eddy simulation of stratified turbulence, Theoret. Comput. Fluid Dynamics 2 (1991) 1279–1290.

[23] J.M. Prusa, P.K. Smolarkiewicz, A.A. Wyszogrodzki, Simulations of gravity wave induced turbulence using 512 PE CRAY T3E, Int. J. Appl. Math. Comput. Sci. 11 (2000) 101–115.

[24] P.K. Smolarkiewicz, W.W. Grabowski, The Multidimensional Positive definite Advection Transport Algorithm: Nonoscillatory Option, J. Comput. Phys. 86 (1990) 355–375.

[25] C.S. Cotter, P.K. Smolarkiewicz, I.N. Szczyrba, A viscoelastic model for brain injuries, Int. J. Numer. Methods Fluids 40 (2002) 303–311.

[26] A. Arakawa, V. Lamb, Computational design of the basic dynamical processes of the UCLA general circulation model, in: J. Chang (Ed.), Methods in Computational Physics, vol. 17, Academic Press, New York, 1977, pp. 174–265.

[27] S.C. Eisenstat, H.C. Elman, M.H. Schultz, Variational iterative methods for nonsymmetric systems of linear equations, SIAM J. Numer. Anal. 20 (1983) 345–357.

[28] P.K. Smolarkiewicz, L.G. Margolin, Variational solver for elliptic problems in atmospheric flows, Appl. Math. Comput. Sci. 4 (1994) 527–551.

[29] W.C. Skamarock, P.K. Smolarkiewicz, J.B. Klemp, Preconditioned conjugate-residual solvers for Helmholtz equations in nonhydrostatic models, Monthly Weather Rev. 125 (1997) 587–599.

[30] Y. Saad, A flexible inner-outer preconditioned GMRES algorithm, SIAM J. Sci. Stat. Comput. 14 (1993) 461–469.

[31] J.M. Prusa, W.J. Gutowski, MPDATA and grid adaptivity in geophysical fluid flow models, Int. J. Num. Methods Fluids 50 (2006) 1207–1228.

[32] P. Bernardet, The pressure term in the anelastic model: a symmetric elliptic solver for an Arakawa C grid in generalized coordinates, Monthly Weather Rev. 123 (1995) 2474–2490.

[33] P.K. Smolarkiewicz, L.G. Margolin, Variational methods for elliptic problems in fluid models, in: Proceedings of ECMWF Workshop on Developments in Numerical Methods for Very High Resolution Global Models 5–7 June; Reading, UK, ECMWF, 2000, pp. 137–159.

[34] P.K. Smolarkiewicz, C. Temperton, S.J. Thomas, A.A. Wyszogrodzki, Spectral Preconditioners for nonhydrostatic atmospheric models: extreme applications, in: Proceedings of the ECMWF Seminar Series on Recent developments in numerical methods for atmospheric and ocean modelling, 6–10 September, Reading, UK, 2004, pp. 203–220.

[35] W.H. Snyder, Similarity criteria for the application of fluid models to the study of air pollution meteorology, Bound. Layer Meteorol. 3 (1972) 113–134.

[36] http://www.mmm.ucar.edu/eulag/Appl_Urban.html.

[37] I. Mavroidis, R.F. Griffiths, D.J. Hall, Field and wind tunnel investigations of plume dispersion around single surface obstacles, Atmos. Environ. 37 (2003) 2903–2918.

[38] A.M. Mfula, V. Kukadia, R.F. Griffiths, D.J. Hall, Wind tunnel modelling of urban building exposure to outdoor pollution, Atmos. Environ. 39 (2005) 2737–2745.

[39] M.F. Yassin, S. Kato, R. Oaka, T. Takahashi, T. Ohtsu, Wind tunnel study on the pollutant dispersion over an urban area, in: Air Pollution X (2002) 625–633.

[40] P.W.M. Brighton, Strongly stratified flow past three-dimensional obstacles, Quart. J. R. Met. Soc. 104 (1978) 289–307.

[41] C.R. Hunt, W.H. Snyder, Experiments on stably and neutrally stratified flow over a model three-dimensional hill, J. Fluid Mech. 96 (1980) 671–704.

[42] P.G. Baines, Topographic Effects in Stratified Flows, Cambridge Univ. Press, Cambridge, 1995, 482 pp.

[43] Y.Q. Zhang, S.P. Ayra, W.H. Snyder, A comparison of numerical and physical modeling of stable atmospheric flow and dispersion around a cubical building, Atmos. Environ. 30 (1996) 1327–1345.

[44] R.G. Frehlich, R.Y. Meillier, M.L. Jensen, B. Balsley, R. Sharman, Measurements of Boundary Layer Profiles in an Urban Environment, J. Appl. Meteor. Clim. 45 (2006) 821–837.

[45] R.B. Smith, Linear theory of stratified hydrostatic flow past an isolated mountain, Tellus 32 (1980) 348–364.

[46] P.K. Smolarkiewicz, R. Rotunno, Low Froude number flow past three-dimensional obstacles. Part I: Baroclinically generated lee vortices, J. Atmos. Sci. 46 (1989) 1154–1164.

[47] P.K. Smolarkiewicz, R. Rotunno, Low Froude number flow past three-dimensional obstacles. Part II: Upwind flow reversal zone, J. Atmos. Sci. 47 (1990) 1498–1511.

[48] C.C. Epifanio, R. Rotunno, The dynamics of orographic wake formation in flows with upstream blocking, J. Atmos. Sci. 62 (2005) 3127–3150.

[49] F.F. Grinstein, L.G. Margolin, W. Rider (Eds.), Implicit large eddy simulation: computing turbulent fluid dynamics, Cambridge University Press, 2007, p. 552.

[50] L.G. Margolin, P.K. Smolarkiewicz, A.A. Wyszogrodzki, Implicit turbulence modeling for high Reynolds number flows, J. Fluids Eng. 124 (2002) 862–867.

[51] J. A Domaradzki, Z. Xiao, P.K. Smolarkiewicz, Effective eddy viscosities in implicit large eddy simulations of turbulent flows, Phys. Fluids 15 (2003) 3890–3893.

[52] L.G. Margolin, P.K. Smolarkiewicz, A.A. Wyszogrodzki, Dissipation in implicit turbulence models: A Computational Study, ASME J. Appl. Mech. 73 (2006) 469–473.

[53] R.D. Sharman, M.G. Wurtele, Ship waves and lee waves, J. Atmos. Sci. 40 (1982) 396–427.

[54] P.K. Smolarkiewicz, J. Szmelter, MPDATA: an edge-based unstructured-grid formulation, J. Comput. Phys. 206 (2005) 624–649.

[55] J. Szmelter, P.K. Smolarkiewicz, MPDATA error estimator for mesh adaptivity, Int. J. Numer. Methods Fluids 50 (2006) 1269–1293.

[56] A.A. Wyszogrodzki, P. Smolarkiewicz, R. Sharman, J. Szmelter, Large-eddy simulations of urban boundary layers, in: 10th Annual George Mason University Conference on Atmospheric Transport and Dispersion Modeling, August 1–3, George Mason University Fairfax, VA, USA, 2006, http://camp.gmu.edu/10th-announcement.html.